The 6dF Galaxy Survey: The Near-Infrared Fundamental Plane of Early-Type Galaxies

Christina Magoulas[1,2], Christopher M. Springob[2], Matthew Colless[2], D. Heath Jones[2,3], Lachlan A. Campbell[4], John R. Lucey[5], Jeremy Mould[6], Tom Jarrett[7], Alex Merson[5], Sarah Brough[2]

[1] *School of Physics, University of Melbourne, Parkville, VIC 3010, Australia*
[2] *Australian Astronomical Observatory, PO Box 296, Epping, NSW 1710, Australia*
[3] *School of Physics, Monash University, Clayton, VIC 3800, Australia*
[4] *Department of Physics & Astronomy, University of Western Kentucky, Bowling Green, KY 42102-3576, USA*
[5] *Department of Physics, University of Durham, Durham DH1 3LE, UK*
[6] *Centre for Astrophysics and Supercomputing, Swinburne University, Hawthorn, VIC 3122, Australia*
[7] *Spitzer Science Center, California Institute of Technology, Pasadena, CA 91125, USA*

Draft version of 2 June 2012

ABSTRACT
We determine the near-infrared Fundamental Plane for $\sim 10^4$ early-type galaxies in the 6dF Galaxy Survey (6dFGS). We fit the distribution of central velocity dispersion, near-infrared surface brightness and half-light radius with a three-dimensional Gaussian model using a maximum likelihood method. The model provides an excellent empirical fit to the observed Fundamental Plane distribution and the method proves robust and unbiased. Tests using simulations show that it gives superior results to regression techniques in the presence of significant and correlated uncertainties in all three parameters, censoring of the data by various selection effects, and outliers in the data sample. For the 6dFGS J band sample we find a Fundamental Plane with $R_e \propto \sigma_0^{1.52\pm0.03} I_e^{-0.89\pm0.01}$, similar to previous near-infrared determinations and consistent with the H and K band Fundamental Planes once allowance is made for differences in mean colour. The overall scatter in R_e about the Fundamental Plane is $\sigma_r = 29\%$, and is the quadrature sum of an 18% scatter due to observational errors and a 23% intrinsic scatter. Because of the Gaussian distribution of galaxies in Fundamental Plane space, σ_r is *not* the distance error, which we find to be $\sigma_d = 23\%$. Using group richness and local density as measures of environment, and morphologies based on visual classifications, we find that the Fundamental Plane slopes do not vary with environment or morphology. However, for fixed velocity dispersion and surface brightness, field galaxies are on average 5% larger than galaxies in groups or higher-density environments, and the bulges of early-type spirals are on average 10% larger than ellipticals and lenticulars. The residuals about the Fundamental Plane show significant trends with environment, morphology and stellar population. The strongest trend is with age, and we speculate that age is the most important systematic source of offsets from the FP, and may drive the other trends through its correlations with environment, morphology and metallicity. These results will inform our use of the near-infrared Fundamental Plane in deriving relative distances and peculiar velocities for 6dFGS galaxies.

Key words: surveys — galaxies:fundamental parameters — galaxies: elliptical and lenticular — galaxies: evolution — galaxies: structure

1 INTRODUCTION

Empirical correlations between observable galaxy parameters guide our understanding of the physical mechanisms that regulate the formation and evolution of galaxies. One of the first early-type galaxy scaling relations was recognised by Faber & Jackson (1976), and connects galaxy luminosity, L, and stellar velocity dispersion, σ. The Faber-Jackson (FJ) relation has the form of a power law,

$L \propto \sigma^\gamma$, where γ is usually observed to be in the range 3 to 5. A similar relation between galaxy luminosity and effective radius, R_e, was derived around the same time (Kormendy 1977). The Kormendy relation also has power-law form, $L \propto R_e^\epsilon$, with ϵ usually found to be in the range -1 to -2. Both relations show a wide range of slopes depending on the properties of the sample under consideration (e.g. absolute magnitude and morphological

type) and substantial intrinsic scatter, in the range 0.2–0.5 dex (e.g. Desroches et al. 2007; Nigoche-Netro, Ruelas-Mayorga & Franco-Balderas 2008; Nigoche-Netro et al. 2010).

However, subsequent examination of the three-dimensional (3D) logarithmic space of size, surface brightness and velocity dispersion revealed that early-type galaxies populate a more tightly correlated two-dimensional (2D) plane with significantly lower intrinsic scatter (Dressler et al. 1987; Djorgovski & Davis 1987). This Fundamental Plane (FP) has the power-law form $R_e \propto \sigma_0^a \langle I_e \rangle^b$, where R_e is the effective radius, $\langle I_e \rangle$ is the mean surface brightness enclosed within the effective radius, and σ_0 is the central stellar velocity dispersion.

Since the original formulation of the FP relation, the size and quality of early-type galaxy samples have been steadily improved (e.g. Bernardi et al. 2003; D'Onofrio et al. 2008; La Barbera et al. 2008; Hyde & Bernardi 2009; Gargiulo et al. 2009; La Barbera et al. 2010b; Graves, Faber & Schiavon 2010) in an effort to explain important properties such as the FP's observed orientation (or *tilt*) and its intrinsic scatter (or *thickness*).

The *tilt* of the FP is the difference between the observed coefficients of the plane, a (for $\log \sigma_0$) and b (for $\log \langle I_e \rangle$), and the values $a = 2$ and $b = -1$ that would follow if galaxies were homologous virialised systems with constant mass-to-light ratio. The physical origin of this tilt is usually interpreted as being due to some combination of systematic deviations either from dynamical homology (i.e. differences in density profile or orbital structure) or from a fixed mass-to-light ratio (M/L). Both effects clearly contribute in some degree, but neither one by itself appears to explain the entirety of the FP tilt, leaving its origin an open and much-debated question (see, e.g., Ciotti, Lanzoni & Renzini 1996; Busarello et al. 1997; Graham & Colless 1997; Trujillo, Burkert & Bell 2004; D'Onofrio et al. 2006; Cappellari et al. 2006).

The other notable property of the Fundamental Plane is its remarkably small intrinsic scatter or *thickness*, which has enabled its use as a distance indicator for early-type galaxies. The intrinsic scatter in the distance-dependent quantity, R_e, is measured to be as small as 10–15%, although the effective precision of the distance estimator, including observational errors, is typically 20–30% (see discussion in §5.8 and Table 4).

Several authors (Scodeggio et al. 1998; Bernardi et al. 2003; Hyde & Bernardi 2009; La Barbera et al. 2010a) have detected a weak steepening of the slope in $\log \sigma_0$ (i.e. a decrease in a) in redder passbands. This wavelength variation has also been observed in near-infrared (NIR) FP samples (e.g. Pahre, Djorgovski & de Carvalho 1998; Jun & Im 2008), suggesting a variation of stellar content (and M/L) along the FP. In contrast, the slope in $\log \langle I_e \rangle$ (i.e. b) is found to be largely independent of wavelength.

The Fundamental Plane relation is often claimed to be 'universal', in the sense that the coefficients are similar for galaxies across environments ranging from the low-density field to high-density clusters (e.g. Jorgensen, Franx & Kjaergaard 1996; Pahre, de Carvalho & Djorgovski 1998; Colless et al. 2001; Reda, Forbes & Hau 2005). However there are also suggestions in the literature that there are mild, but statistically significant, environmental variations (e.g. Lucey, Bower & Ellis 1991; de Carvalho & Djorgovski 1992; Bernardi et al. 2003; D'Onofrio et al. 2008; La Barbera et al. 2010c). Any variation in the FP between field and cluster galaxies, or for galaxies in clusters of different richness, would be interesting from the point of view of the formation of early-type galaxies, but would complicate the use of the FP as a distance indicator.

The structural similarity of elliptical (E) galaxies and the bulges of lenticular (S0) and early-type spiral galaxies suggests that the latter classes of object may also populate the FP (Dressler et al. 1987), and Jorgensen, Franx & Kjaergaard (1996) found that the FPs for E and S0 galaxies were consistent. In contrast, galaxies with both bulge *and* disk components have been observed to be offset from ellipticals on the FP (Bender, Burstein & Faber 1992; Saglia, Bender & Dressler 1993). It is therefore important to examine whether there are morphological variations in the observed FP, and (if so) whether these are due to intrinsic differences between E's and the bulges of S0's and early-type Sp's or to observational contamination of the bulge parameters by the disk for the latter classes of galaxy. If such morphological variation exists, for either reason, it would result at some level in offsets and increased scatter of the FP, and increase the systematic and random errors (respectively) in the estimated distances and peculiar velocities.

More recent studies (Graves, Faber & Schiavon 2009; La Barbera et al. 2010a) have focused on the trends in FP space of stellar population parameters such as age and metallicity. A separate paper in this series (Springob et al. 2012) explores the variations of age and metallicity within the 6dFGS FP sample, and looks for variations of the FP for galaxies with different stellar populations.

One difficulty in comparing the results from different studies of the FP is that physical variations can be mimicked by biases resulting from the interaction of the fitting method with the sample selection criteria or the complicated error dependencies in the data. The regression methods typically used to fit the FP broadly fall in the category of linear least squares, and minimise the residuals of one of the FP variables or the residuals orthogonal to the plane. The type of least-squares regression chosen is often determined by the focus of the study (e.g. regression on $\log R_e$ to estimate distances or regression on $\log \langle I_e \rangle$ for a stellar population study), though it is well-known that different regression methods do not necessarily converge on a unique (or even consistent) best fit, particularly if selection effects or correlated measurement errors are not fully accounted for (Hogg, Bovy & Lang 2010). This tendency to use different regression techniques interchangeably has made it challenging to compare the results of different FP studies, and in some cases has led to conclusions that are either incorrect or misleading.

There is also the additional question of whether the traditional FP model of a 2D plane with Gaussian scatter is statistically robust or truly representative of the distribution of galaxies in FP space. Saglia et al. (2001) have shown that a 3D Gaussian model provides a more accurate (and therefore less biased) representation of the galaxy distribution, at least for the large, bright, early-type galaxies in most FP samples.

Given these considerations, we have developed a robust maximum likelihood algorithm for fitting the galaxy distribution in FP space with a 3D Gaussian model. Through simulations we compare this approach to the usual least-squares regressions of a plane with Gaussian scatter, and show that it is superior in virtually all respects: more versatile in dealing with complex sample selection criteria and correlated measurement errors, more robust against outliers and blunders in the data, and providing unbiased and precise estimates of the FP parameters and their uncertainties.

We apply this method to a sample of $\sim 10^4$ early-type galaxies drawn from the 6-degree Field Galaxy Survey. The 6dFGS is a combined redshift and peculiar velocity survey of galaxies covering the entire southern sky at $|b| > 10°$ (Jones et al. 2004, 2005, 2009). The FP sample consists of the brightest (highest S/N) ellipticals, lenticulars and early-type spiral bulges in the 6dFGS volume out to $cz = 16,500\,\mathrm{km\,s^{-1}}$. This sample will ultimately form the basis of the 6dFGS peculiar velocity survey (6dFGSv), with the broad aims of mapping the density and velocity fields in the nearby

Universe and providing tighter constraints on a range of cosmological parameters (Colless et al. 2005).

The paper is organised as follows. Section 2 outlines the general 3D Gaussian model and maximum likelihood algorithm that can be used to fit any FP sample. Section 3 describes the FP sample data from the 6dFGS to which we apply our model. We establish the validity of our methodology and determine the errors on the fits from Monte Carlo simulations using mock samples described in Section 4. The overall FP fit results are given in Section 5; variations of the FP with environment are addressed in Section 6 and dependencies on galaxy morphology in Section 7. Various aspects of our results are discussed in Section 8, including: the validity of modelling the FP as a 3D Gaussian; the interpretation of the scatter about the FP and the proper estimation of distance errors; the physical insights offered by studying the FP in κ-space; and the significance of the trends of the residuals about the FP with environment, morphology and stellar population. Throughout we assume a flat ΛCDM cosmology with $\Omega_m = 0.3$, $\Omega_\Lambda = 0.7$ and $H_0 = 100\, h\, \mathrm{km\ s^{-1}\ Mpc^{-1}}$; this is only used for converting between angular and physical scales, and in fact the specific cosmology chosen makes little difference for this low-redshift sample.

2 MAXIMUM LIKELIHOOD GAUSSIAN FIT

2.1 Motivation

The Fundamental Plane relation is defined as

$$\log R_e = a \log \sigma_0 + b \log \langle I_e \rangle + c \qquad (1)$$

where the coefficients a and b are the *slopes* of the plane and the constant c is the *offset* of the plane. In this study we employ units of h^{-1} kpc for effective radius R_e, km s^{-1} for central velocity dispersion σ_0, and L$_\odot$ pc^{-2} for mean surface brightness $\langle I_e \rangle$. We prefer to use $\log \langle I_e \rangle$ rather than $\langle \mu_e \rangle$ (which is in units of mag arcsec^{-2}), so that all our FP parameters are unscaled logarithmic quantities; this means that the relative errors and scatter are directly comparable in all axes. Throughout the rest of this paper we adopt an abbreviated notation for the FP parameters: $r \equiv \log R_e$, $s \equiv \log \sigma_0$ and $i \equiv \log \langle I_e \rangle$. Hence we write the FP relation as

$$r = as + bi + c \,. \qquad (2)$$

Traditional methods for deriving the coefficients of equation 1 have preferred using a form of linear regression that involves minimising residuals in the direction of one of the FP axes (Dressler et al. 1987), or orthogonal to the plane itself (Jorgensen, Franx & Kjaergaard 1996), or both (Hyde & Bernardi 2009; La Barbera et al. 2010a). Least-squares is used for its simplicity and relatively fast numerical implementation. However, such regression techniques can be biased by the choice of variable they minimise, the unacknowledged properties of the model they assume, the selection effects they fail to model, and the (possibly correlated) uncertainties they do not include in the fit. Simple regressions are thus likely to result in unreliable and biased fits to the FP.

Specifically, we identify the dominant sources of bias in FP samples as arising in general from: (i) the model for the FP distribution and its intrinsic scatter; (ii) selection effects, in the form of both hard and soft censoring of the sample; and (iii) the measurement errors on all three FP variables, which are often correlated.

(i) *FP distribution model:* As discussed above, a 3D Gaussian is a simple and convenient model that empirically is found to be a better match to the (censored) observed FP distribution of early-type galaxies than the standard model of a 2D plane-surface with

Gaussian scatter in one direction (see §4.1). The standard model effectively assumes that galaxies uniformly populate the whole plane, whereas the 3D Gaussian naturally accounts not only for the scatter about the plane but also the distribution within the plane, at least for the bright galaxies included in the 6dFGS sample and most others.

(ii) *Selection effects:* Censoring of the intrinsic FP distribution is always present for observed FP samples, in both obvious and not-so-obvious ways. If the fitting technique is to avoid biased results due to censoring, it must account for all the selection effects. These include both hard selection limits in FP variables (e.g. in velocity dispersion due to the limiting instrumental resolution) or soft (i.e. graduated) selection limits in any other observable or combination of observables (e.g. the joint selection on size and surface brightness due to the flux limit of a sample). Using maximum likelihood fitting it is straightforward to incorporate these limits (see §2.5); by comparison, for linear regressions it is significantly more difficult to account for selection effects more complex than a hard limit in one variable.

(iii) *Measurement errors:* The modelling of measurement errors in a FP sample is complicated by the fact that galaxies have different errors in all three of their FP parameters, and some of these errors are significantly correlated (notably those in r and i). Standard least-squares regression only accounts for uncorrelated measurement errors (and in naive applications, only measurement errors in one parameter). However, a maximum likelihood approach can account exactly for differing measurements errors and their correlations in a straightforward way.

2.2 Least-Squares Regression Bias

As discussed above, a maximum likelihood method is clearly to be preferred in principle. However it does not necessarily follow in practice that the limitations of the linear regression approach result in significant biases when fitting the FP. We therefore illustrate the consequences of using linear regressions to fit mock samples simulated by drawing galaxies from a 3D Gaussian intrinsic FP and applying realistic measurement errors and selection effects. The process of creating these mock samples is outlined in Section 4.1.

Three different types of mock samples were fit with each of the commonly-used linear least-squares regressions (i.e. by minimising residuals in the distance-dependent quantity, $X_{\mathrm{FP}} \equiv r - bi$, or the distance-independent quantity, $\log \sigma_0 \equiv s$, or the residuals orthogonal to the regression line) and also by a maximum likelihood fit of a 3D Gaussian. In the lefthand panels of Figure 1 we compare the fits to these mocks using the observed effective radius versus predicted effective radius (calculated from equation 2). The simplest mock sample, panel (a) and panel (e), is just the intrinsic distribution with no observational errors or selection effects applied to it; consequently it is the tightest sample and the best fit has almost no method-dependent bias.

However, when simulated observational error scatter is added to the mock FP parameters, panel (b), the sample is significantly skewed away from the one-to-one line as a result of the systematic variation in the observational errors with velocity dispersion, size and surface brightness, as well as the correlation between the observational errors in size and surface brightness. The skewing effect is exacerbated when censoring is also present in the mock sample; panel (c) shows the situation where the censored data is absent, while panel (d) is the same but with the censored data shown in red (though still not included in the fits). This censoring is the result of observational selection effects operating on both velocity dispersion (due to the instrumental spectral resolution limit) and
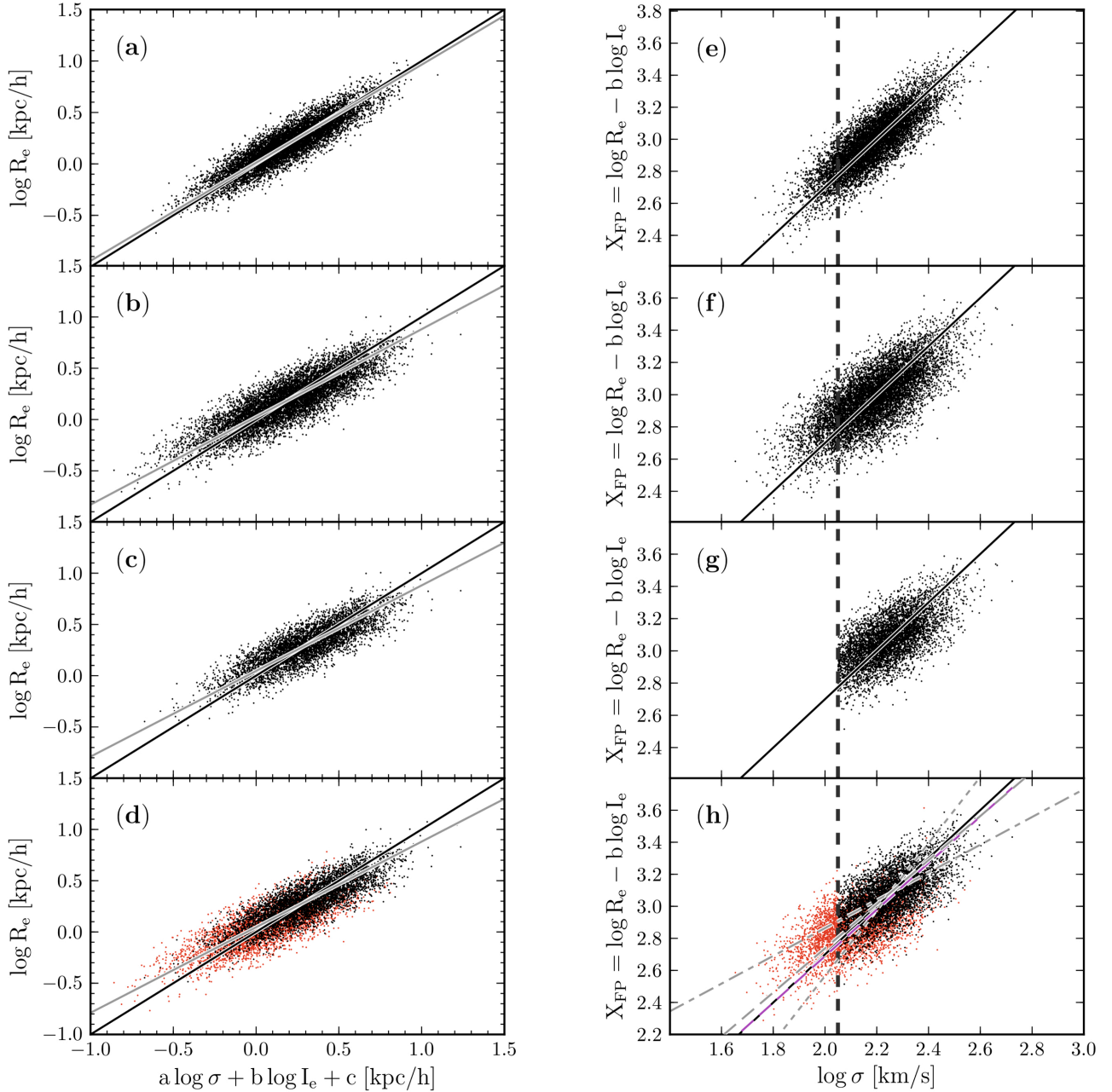
Figure 1. *Panels (a)–(d):* Comparison of the observed effective radius against predicted effective radius (calculated from equation 2) for mock samples all with the same underlying FP ($r = 1.52s - 0.89i - 0.33$) and intrinsic scatter, but subject to differing levels of measurement errors and sample censoring: (a) no measurement errors or censoring ($N_g = 8901$); (b) measurement errors but no censoring ($N_g = 8901$); (c) both measurement errors and censoring ($N_g = 5139$); (d) as for (c) but with the censored data points shown in red ($N_g = 8901$). Note that the sample is skewed from the one-to-one line (in black) by the measurement errors and the censoring of the sample, as indicated by the best-fit orthogonal regression lines for each sample (in grey). *Panels (e)–(h):* For the same mock samples as in (a)–(d), the correlation between the distance-dependent quantity, $X_{FP} \equiv r - bi$, and the distance-independent quantity, $s \equiv \log \sigma_0$. The vertical dashed black line indicates the hard cut in $\log \sigma_0$ ($s \geqslant 2.05$) that is applied, along with other selection cuts, in censoring the mock samples in panels (g) and (h). In each panel the solid black line indicates the intrinsic FP that the mock samples were generated from; panel (h) also shows as grey lines the standard least-squares regressions (in 2D) minimising with respect to X_{FP} (dot-dash) and s (dotted), and the orthogonal regression (dashed); the solid magenta line shows the maximum likelihood fit to a 3D Gaussian.

jointly on size and surface brightness (due to the sample apparent magnitude limit). The consequences of this skewing of the sample distribution are illustrated in panels (a)–(d) by the discrepancy between the 1-to-1 relation (black line) and the best-fit orthogonal regression (grey line). The overall effect, shown in panels (c) and

(d), is that the best-fit slope is found to be 0.84 rather the true value of unity.

This biasing is also seen in the frequently used 2D projection of the FP showing the distance-dependent photometric parameter, $X_{FP} \equiv r - bi$, and distance-independent spectroscopic parameter, $s \equiv \log \sigma_0$. The righthand panels in Figure 1 show this projec-

tion for precisely the same mock FP samples as those in the corresponding lefthand panels. The most obvious selection effect on the mock sample in the righthand bottom panel is the velocity dispersion limit, which censors the red points to the left of the vertical dashed line at $s = 2.05$ (i.e. $\log \sigma_0 = 112\,\mathrm{km\,s^{-1}}$). The red points to the right of this line are those eliminated by the joint selection effect on r and i due to the apparent magnitude limit of the sample, which tends to censor galaxies with smaller sizes and fainter surface brightnesses, but in a way that depends on redshift.

These simulations show that the combined effect from all the selection criteria and measurement errors skews the best fit when not accounted for correctly (as is the case for least-squares fitting), most noticeably for the regressions on X_{FP} and s. The orthogonal fit (dashed grey line) fits the data well in this projection, but this is a consequence of fixing the value of b, a priori, to approximately the correct value. In this case, b has been fixed to the canonical value of $b = -0.75$; because this differs from the input value of $b = -0.88$ for the mock sample, the fit deviates from the input plane (particularly at the low-σ end). Additionally, Figure 1 illustrates why the maximum likelihood best fit does not appear, by eye, to be a good fit to the observed data—the observational errors and the selection effects systematically skew the observed sample away from the underlying intrinsic distribution.

The conclusion from this exercise is that, for samples with realistic observational errors and censoring, the input FP is best recovered with the maximum likelihood method. Regressions on X_{FP} or s lead to highly biased results, while the 2D orthogonal regression gives a reasonable fit, at least for this particular combination of observables, only if b is fixed a priori close to the true value. However, as shown below, regressions on r, s, i and the orthogonal residuals *all* show significant biases when fitting the FP parameters in 3D, and only the maximum likelihood method accurately recovers the FP.

To illustrate the differences resulting from different fitting methods in 3D and the impact of various problems with the real data, we fit simulated samples with progressively more realistic properties (just as in Figure 1). Figure 2 shows the fitted FP slope values (a and b) for 1000 mock samples of various types (each sample containing 8901 galaxies) using least-squares regression in 3D on each of the FP variables (i.e. r, s, i) and orthogonal to the plane, as well as our 3D Gaussian model fitted using a maximum likelihood method. In green are the results of fits to mocks just including the intrinsic scatter of the FP; in blue are the fits to mocks with both intrinsic scatter and sample censoring due to the selection criteria; and in red are fully realistic mocks including all the effects of intrinsic scatter, selection criteria and observational errors.

The linear regressions on individual FP parameters give biased estimates of a and b even for the 'ideal' case (green), and become progressively more strongly biased as censoring and observational errors are included (blue and red). The $\log \sigma_0$ slope, a, is biased high, even for the 'ideal' case, when an FP sample is fit by minimising the $\log \sigma_0$ residuals as compared to the other fitting techniques. This is consistent with previous studies (Jorgensen, Franx & Kjaergaard 1996; La Barbera et al. 2010a) and is a result of the dominant selection limit in $\log \sigma_0$. The sense of the trends in both a and b for all regression methods agree with those found by Saglia et al. (2001), as shown in their Figure 6.

Figure 2 also indicates that orthogonal regression (in 3D) is the least biased of the regression methods; however, in the most realistic simulations (red), it nonetheless returns slopes that are biased by many times the nominal precision of the fits (given by the 1σ contour). The maximum likelihood fitting method clearly out-performs

all the regression methods, recovering the FP slopes without significant bias for *all* types of mock samples (see the inset, which expands the region centred on the input values of the FP slopes).

As might be expected, for all fitting methods the error contours on the fitted slopes become larger when censoring and observational errors are applied to the mock samples. Not so obviously, the error contours for the most realistic mocks (red) are largest for the maximum likelihood fit and the regression on s; the apparently greater precision of the r, i and orthogonal regressions are obtained at the expense of very substantial biases in the fitted slopes. These regression fits thus give a false sense of precision while at the same time introducing biases that are many times larger than the nominal errors on the fitted slopes.

2.3   3D Gaussian Likelihood Function

The Fundamental Plane is modelled as a three-dimensional Gaussian in a similar fashion to the approach adopted by the EFAR survey (Saglia et al. 2001; Colless et al. 2001) and subsequently by Bernardi et al. (2003). This choice of model is justified by the good empirical match it provides to the distribution of galaxies in FP space, at least for samples limited by their selection criteria to larger, brighter galaxies.

In one dimension the Gaussian probability distribution for a given galaxy, n, is

$$P(x_n) = \frac{1}{\sqrt{2\pi\sigma^2}} \exp -\frac{(x_n - \bar{x})^2}{2\sigma^2} \qquad (3)$$

for a variable, x_n, with mean $\bar{x}$ and standard deviation σ. Generalising this to three dimensions, the probability density distribution, $P(\mathbf{x_n})$, for a given galaxy, n, occupying the position $\mathbf{x_n} = (r - \bar{r}, s - \bar{s}, i - \bar{i})$ in FP space with respect to the mean values $\bar{r}$, $\bar{s}$ and $\bar{i}$ is

$$P(\mathbf{x_n}) = \frac{\exp[-\frac{1}{2}\mathbf{x_n^T}(\mathbf{\Sigma} + \mathbf{E_n})^{-1}\mathbf{x_n}]}{(2\pi)^{\frac{3}{2}}|\mathbf{\Sigma} + \mathbf{E_n}|^{\frac{1}{2}} f_n} \qquad (4)$$

where f_n is the normalisation factor accounting for the fact that, due to selection effects, the galaxies do not fully sample the entire Gaussian distribution. The total 3D scatter in FP space is given by the addition of the FP variance matrix, $\mathbf{\Sigma}$ (specifying the intrinsic scatter of the FP distribution in 3D) and the observational error matrix $\mathbf{E_n}$ (specifying the observational errors in r, s and i and their correlations; this is constructed in §3.3).

The Fundamental Plane space can be described either in terms of the observational parameters or in terms of the unit vectors showing the principal axes of the 3D Gaussian characterising the galaxy distribution (hereafter, $\mathbf{v}$-space). The Fundamental Plane itself is defined by its normal vector, which is the eigenvector of the intrinsic FP variance matrix $\mathbf{\Sigma}$ with the smallest eigenvalue. A representation of the $\mathbf{v}$-space axes ($\mathbf{v_1}, \mathbf{v_2}, \mathbf{v_3}$) with respect to the axes of the observational parameters (r, s, i) is shown in Figure 3 as a 3D interactive visualisation that can be accessed by viewing this paper in Adobe Reader Version 8.0 or higher. All the interactive 3D figures in this paper were created with custom C-code and the S2PLOT graphics library (Barnes et al. 2006), using the approach described in (Barnes & Fluke 2008).

The resulting vectors that define the axes of the Gaussian are

$$\hat{\mathbf{v}}_{\mathbf{1}} = (1/\sqrt{1 + a^2 + b^2}) \cdot \mathbf{v_1} \,,$$
$$\hat{\mathbf{v}}_{\mathbf{2}} = (b/\sqrt{1 + b^2}) \cdot \mathbf{v_2} \,, \qquad (5)$$
$$\hat{\mathbf{v}}_{\mathbf{3}} = (ab/\sqrt{(1 + b^2)(1 + a^2 + b^2)}) \cdot \mathbf{v_3} \,,$$
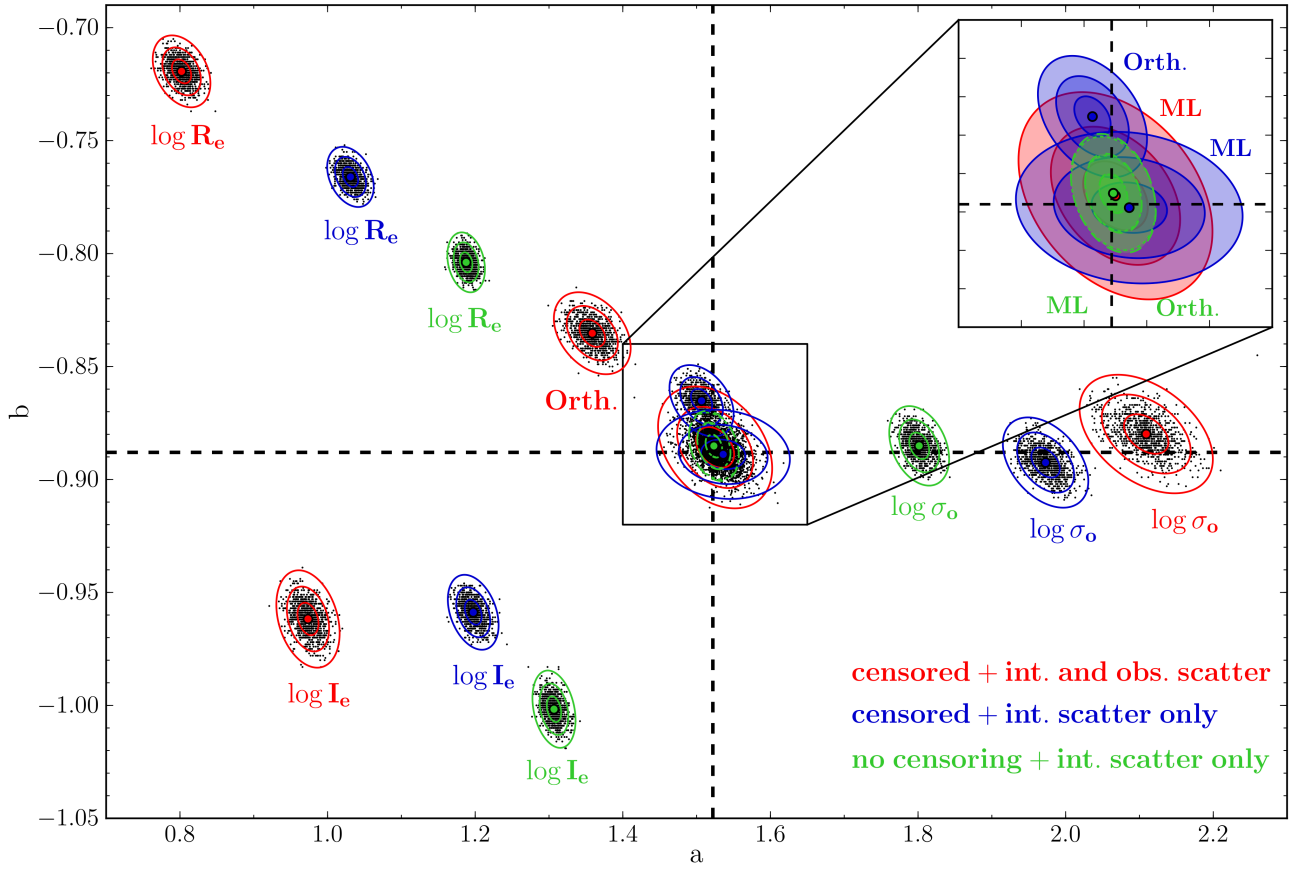
Figure 2. The best-fit values for the FP slopes, a and b, for each of 1000 mock FP samples (black dots) fit with least-squares regressions (in 3D) minimising the residuals in each of the three FP variables (i.e. r, s, i) and orthogonal to the plane; also fit with the maximum likelihood 3D Gaussian. The labels on each cluster of black points indicate the fitting method used; the colours indicate whether intrinsic scatter, observational errors and selection effects (censoring) are included in the mock samples, as follows: green indicates the mocks only include the intrinsic scatter of the FP; blue indicates the mocks include intrinsic scatter and censoring; red indicates the mocks include intrinsic scatter, observational scatter and censoring. The mean values of the fitted slopes (coloured dots) and the 1σ, 2σ and 3σ contours (coloured ellipses) are over-plotted in the colour corresponding to the type of mock sample. The dashed lines indicate the input FP coefficients ($a = 1.52$ and $b = -0.89$) from which all the mock samples were drawn.

where

$$\mathbf{v_1} = \hat{\mathbf{r}} - a\hat{\mathbf{s}} - b\hat{\mathbf{i}} \,,$$

$$\mathbf{v_2} = \hat{\mathbf{r}} + \hat{\mathbf{i}}/b \,, \qquad (6)$$

$$\mathbf{v_3} = -\hat{\mathbf{r}}/b - (1 + b^2)\hat{\mathbf{s}}/(ab) + \hat{\mathbf{i}} \,,$$

in terms of the FP slopes a and b. These are the same axes defined by Colless et al. (2001) for the EFAR FP study, with the exception that the value of b quoted in this study is the coefficient of $\log\langle I_e \rangle$ (with units of $L_\odot \, \mathrm{pc}^{-2}$) rather than the coefficient of $\langle \mu_e \rangle$ (with units of $\mathrm{mag\,arcsec}^{-2}$) used in the EFAR study, so that $b_{6dF} = -2.5\, b_{EFAR}$.

The direction of the short axis ($\hat{\mathbf{v}}_1$), which runs *through* (i.e. normal to) the plane, is fully determined by the fitted slopes a and b. The long axis ($\hat{\mathbf{v}}_2$), which runs *along* the plane, is fixed by being orthogonal to $\hat{\mathbf{v}}_1$ and having no $\log\sigma_0$ component. Although this is fixed by fiat, in fact (as we show in Section 5.4) this is very close to the longest natural axis of the 3D Gaussian if no constraints are placed on its direction. The advantage of this definition of $\hat{\mathbf{v}}_2$ lies in its physical interpretation as the direction within the FP that has no dynamical component, connecting only the photometric parameters r and i. The third, intermediate axis ($\hat{\mathbf{v}}_3$), which runs *across* the plane, is orthogonal to both $\hat{\mathbf{v}}_1$ and $\hat{\mathbf{v}}_2$.

Figure 3 also shows the relation between the **v**-space axes and

the physical quantities of dynamical mass (M), luminosity (L), mass-to-light ratio (M/L) and luminosity density (L/R^3). The logarithm of these quantities can be expressed as a function of the FP parameters, under the assumption of homology, as $m = r + 2s$ and $l = 2r + i$, where $m \equiv \log M$ and $l \equiv \log(L)$. The logarithm of mass-to-light ratio is then simply $m - l = -r + 2s - i$ and the logarithm of luminosity density is $l - 3r = -r + i$. Therefore, in the case of the virial plane, where $a = 2$ and $b = -1$, the principal axes are aligned with these quantities: $\mathbf{m} - \mathbf{l} = -\mathbf{v_1}$ and $\mathbf{l} - 3\mathbf{r} = -\mathbf{v_2}$. Even for the actual *tilted* FP we find the angle between these vectors is small (our observed FP has $\mathbf{v_1}$ offset $5.0°$ from $\mathbf{m} - \mathbf{l}$ and $\mathbf{v_2}$ offset $3.6°$ from $\mathbf{l} - 3\mathbf{r}$).

The likelihood function, $\mathcal{L}$, is evaluated from the product of the probability density function (equation 4) for each galaxy, n, using

$$\mathcal{L} = \prod_{n=1}^{N_g} P(\mathbf{x_n})^{1/S_n} \,. \qquad (7)$$

The probability density function is weighted by the fraction of the survey volume in which the galaxy could have been observed, which is inversely proportional to the selection probability, S_n, depending on the magnitude and redshift selection criteria imposed on the FP sample (see §2.5). The probability is normalised over
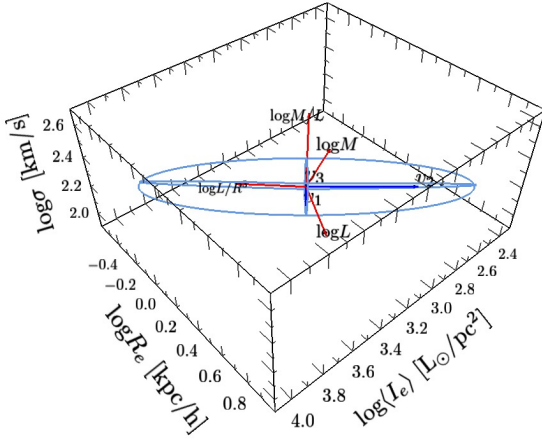
Figure 3. An interactive 3D schematic of FP space, showing the vectors $\mathbf{v_1}, \mathbf{v_2}, \mathbf{v_3}$ (in dark blue) that define the axes (see equation 5) of our Gaussian model (3σ Gaussian ellipsoid in cyan) as they are oriented with respect to the three observational parameter axes $\mathbf{r}, \mathbf{s}, \mathbf{i}$. We also show (in red) the vectors corresponding to the physical quantities $\log M$, $\log L$, $\log M/L$ and $\log L/R^3$ as defined in §2.3. We note that the angle between the vectors $\log M/L$ and $-\mathbf{v_1}$ and also $\log L/R^3$ and $-\mathbf{v_1}$ are both within $5°$ of each other. (Readers using Acrobat Reader v8.0 or higher can enable interactive 3D viewing of this schematic by mouse clicking on the figure; see Appendix B for more detailed usage instructions.)

the region of the FP space allowed by the selection criteria, so that $\int P(\mathbf{x})\, d^3\mathbf{x} = 1$.

For convenience, the log-likelihood value ($\ln \mathcal{L}$) is used, so the product in equation 7 can be reduced to a summation, and then evaluated for our particular $P(\mathbf{x_n})$:

$$\ln \mathcal{L} = -\sum_{n=1}^{N_g} S_n^{-1}\Big[\frac{3}{2}\ln(2\pi) + \ln(f_n) \\ + \frac{1}{2}\ln(|\mathbf{\Sigma} + \mathbf{E}_n|) + \frac{1}{2}\mathbf{x^T}_n(\mathbf{\Sigma} + \mathbf{E}_n)^{-1}\mathbf{x}_n\Big] . \tag{8}$$

The leading factor in the summation is the weight of the nth galaxy, given by the inverse of its selection probability. Within the square brackets, the first three terms are the normalisation of the probability, and the final term is half the χ^2.

2.4 Likelihood Function Optimisation

The log-likelihood of equation 8 is maximised to simultaneously fit for the eight FP parameters that define the 3D Gaussian model discussed in the preceding section. The parameters that are derived from the fit are: the slopes of the plane (a and b, which define the directions of the 3D Gaussian's axes through equation 5); the centre of the 3D Gaussian in FP space ($\bar{r}, \bar{s}, \bar{i}$), which can be used to calculate the offset of the FP ($c = \bar{r} - a\bar{s} - b\bar{i}$); and the dispersion of the Gaussian in each of the three axes ($\sigma_1, \sigma_2, \sigma_3$). The set of parameters $\{a, b, \bar{r}, \bar{s}, \bar{i}, \sigma_1, \sigma_2, \sigma_3\}$ that maximise the log-likelihood of the 3D Gaussian are therefore those that define the best-fit model to the FP data. Note that the offset of the FP, c, is defined in terms of these parameters as $c = \bar{r} - a\bar{s} - b\bar{i}$.

The log-likelihood function is maximised with a non-

derivative multi-dimensional optimisation algorithm called BOBYQA (Bound Optimisation BY Quadratic Approximation; Powell 2006). BOBYQA is found to be more robust and efficient than more generic optimisation algorithms such as the Nelder-Mead simplex algorithm (Nelder & Mead 1965). It performs well under the particular demands of FP fitting, namely high dimensionality (simultaneous optimisation of eight parameters) and large sample size ($\sim 10^4$ galaxies). The parameters in the BOBYQA algorithm that can be tuned to suit the particular function being optimised are the initial and final tolerances, ρ_{beg} and ρ_{end}, and the number of interpolation points between each iteration, N_{int}. After considerable experimentation, values of these parameters that were found to be efficient and to give the required accuracy were $\rho_{beg} = 10^{-1}$, $\rho_{end} = 10^{-5}$ and $N_{int} = 30$. The BOBYQA algorithm with these parameters was used for all the fitting presented in this work.

2.5 Selection Criteria and Fitting

Fundamental Plane studies must employ some form of model to analyse censored or truncated data resulting from observational selection effects. If these models fail to account for statistical effects that are due to selection, they run the risk of biasing the fitting method being used to recover the FP. We now describe the dominant selection limits—both hard and graduated—that pertain to FP data and how a maximum likelihood fitting method can account for this censoring in a straightforward and transparent manner.

A central velocity dispersion lower limit is typical of FP surveys, which are unable to measure dispersions accurately below the instrumental resolution of the spectrograph. Because this limit is applied to just one of the FP parameters (i.e. s), the appropriate 3D Gaussian normalisation is calculated by integrating over the volume of the distribution that remains after the velocity dispersion cut, as outlined in Appendix A. In this way the likelihood is appropriately normalised and the maximum likelihood method correctly accounts for the truncation of the FP in velocity dispersion by this hard selection limit.

Most FP samples are drawn from flux-limited surveys, excluding galaxies fainter than some apparent magnitude limit. This selection effect can be accounted for by weighting the individual likelihood of each galaxy by the inverse of its selection probability S; this is analogous to a $1/V_{max}$ weighting (Schmidt 1968).

For the case of a FP survey with explicit redshift limits, the selection probability is proportional to the fraction of the survey volume between these limits over which a particular galaxy can be observed given the survey's apparent magnitude limit. This is a function of the limiting distance D_n^{lim} (in h^{-1} Mpc) out to which the galaxy n, with an absolute magnitude M_n, can be observed given the survey magnitude limit m^{lim} in a given passband, and can be calculated as

$$D_n^{lim} = 10^{0.2(m^{lim} - M_n - 25)} . \tag{9}$$

If the redshift cz_n^{lim} corresponding to this luminosity distance is larger (smaller) than the high (low) redshift limit of the survey, cz_{max} (cz_{min}), then a galaxy with that absolute magnitude will definitely have been observed (or not) and the selection probability is $S = 1$ (0). However, if cz_n^{lim} is between the minimum and maximum survey redshifts, then the selection probability is given by the fractional co-moving volume in which it *could* be observed given the apparent magnitude limit. Therefore the selection probability

function is

$$S_n = \begin{cases} 1 & cz_n^{lim} \geqslant cz_{max} \\ \frac{V(cz_n^{lim}) - V(cz_{min})}{V(cz_{max}) - V(cz_{min})} & cz_{min} < cz_n^{lim} < cz_{max} \\ 0 & cz_n^{lim} \leqslant cz_{min} \end{cases} \quad (10)$$

where $V(cz)$ is the co-moving volume of the survey out to redshift cz. This definition of S_n is similar to the selection probability of the EFAR survey, although their selection probability function was based on a size parameter rather than absolute magnitude (Saglia et al. 2001).

In addition to these selection effects, a FP sample may contain spurious outliers whose significance is best characterised by a χ^2 value. The χ^2 for a particular galaxy n can be calculated as

$$\chi_n^2 = \mathbf{x_n^T}(\mathbf{\Sigma} + \mathbf{E}_n)^{-1}\mathbf{x}_n \ . \quad (11)$$

Note that this is twice the exponent of the Gaussian probability distribution of equation 4 and appears in the final term of equation 8. Thus χ^2 measures the departure of a galaxy in FP-space from a given 3D Gaussian model, and outliers can be identified and removed based on their extreme (and extremely unlikely) values of χ^2. The refined sample, excluding these high-χ^2 outliers, can then be re-fitted to achieve an improved fit that is not biased by outliers.

3 6DFGS FUNDAMENTAL PLANE DATA AND SAMPLE

3.1 Fundamental Plane data

The 6-degree Field Galaxy Survey (6dFGS) provides a comprehensive census of galaxies and measured redshifts in the Southern hemisphere out to a depth of $z \sim 0.15$ (Jones et al. 2004, 2005). Primary targets were selected from the K band photometry of the Two Micron All Sky Survey (2MASS) Extended Source Catalog (Jarrett et al. 2000), with secondary samples selected to approximately equivalent limits in the 2MASS J and H bands and the SuperCOSMOS (Hambly et al. 2001) r_F and b_J bands. The total apparent magnitude limits of the 6dFGS are $(K, H, J, r_F, b_J) \leqslant$ (12.65, 12.95, 13.75, 15.60, 16.75). The survey extends across the entire southern sky and, because of its near-infrared selection, reaches down to 10 degrees from the Galactic Plane in J, H and K (for b_J and r_F the survey reaches down to 20 degrees from the Galactic Plane). It is the largest combined redshift *and* peculiar velocity survey by a factor of two, with the additional advantage of homogeneous sampling of the galaxy population over a large volume of the local universe.

We initially select galaxies suitable for the 6dFGS peculiar velocity subsample (6dFGSv) from the parent redshift survey sample (6dFGSz) by selecting galaxies with reliable redshifts (i.e. redshift quality $Q = 3 - 5$) and redshifts less than 16500 km s^{-1} (i.e. $z < 0.055$). The redshift limit is imposed because at higher redshifts the key spectral features used to measure $\log \sigma_0$ are shifted out of the wavelength range for which sufficiently high resolution spectra are available (Campbell 2009). These criteria select $\sim$43,000 of the $\sim$125,000 galaxies in the 6dFGS redshift survey.

The spectra of these galaxies is classified by matching the observed spectrum, via cross-correlation, to template galaxy spectra. The sample only includes galaxies with spectra that, within the 6dF fibre region, are a better match to early-type spectral templates (E/S0 galaxies) than to late-type templates (Sbc or later). The sample can therefore be characterised in spectral terms as galaxies that, within the 6dF fibre region, have dominant old stellar populations
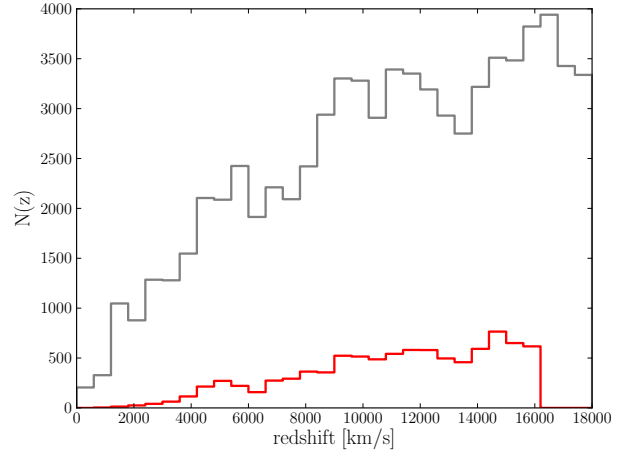

Figure 4. Redshift distribution of the 6dFGSv FP sample (red; N_g=8901) with maximum redshift cz_{max}=16120 km s^{-1} compared to the full 6dFGS redshift sample (grey; N_g=124646).

with little or no ongoing star-formation. Morphologically the sample galaxies are either ellipticals and lenticulars or early-type spirals with the bulge filling the 6dF fibre.

These $\sim$20,000 early spectral type galaxies had their central velocity dispersions measured using the Fourier cross-correlation technique (Campbell 2009). These velocities were then corrected for the effect of the fibre aperture size to a uniform $\log R_e/8$ aperture following the formula of Jorgensen, Franx & Kjaergaard (1995). The sample of galaxies with early-type spectra, sufficiently high signal-to-noise ratio for reliable velocity dispersion measurements ($S/N > 5\,\text{Å}^{-1}$), and velocity dispersions greater than the instrumental resolution limit ($s \geqslant 2.05$, i.e. $\sigma_0 \geqslant 112$ km s^{-1}) contains 11,561 galaxies.

The FP photometric parameters (R_e and $\langle \mu_e \rangle$) for our sample were derived from 2MASS. The relatively large 2MASS point-spread function (PSF), with FWHM $\approx 3.2''$, required a procedure to derive PSF-corrected parameters. For each galaxy we analysed the pixel data provided by the 2MASS Extended Source Image Server as follows. We adopted the apparent magnitude (m) measured by 2MASS from the 'fit extrapolation' method (i.e. j_m_ext, h_m_ext, k_m_ext) and determined the circular apparent half-light radius (r_{APP}) of the target galaxy on the 2MASS image. A model 2D Gaussian PSF image was derived from stars on the parent 2MASS data 'tile'. GALFIT (Peng et al. 2002) was run with the galaxy image and model PSF image as inputs to find the best-fit 2D Sérsic model. The half-light radius was determined for the Sérsic model before and after convolution with the PSF (r_{MODEL} and r_{SMODEL}). The difference $r_{SMODEL} - r_{MODEL}$ is subtracted from r_{APP} to derive the PSF-corrected half-light radius (i.e. the effective radius R_e). The effective radius was observed in angular units of arcseconds, R_e^θ, and converted to physical units of h^{-1} kpc, R_e, using the galaxy's angular diameter distance, $D_A(z)$.

The 2MASS data for the J, H and K bands were analysed independently. As the 2MASS PSF is well-determined and we only use the Sérsic model to provide the PSF-correction, this procedure is very robust. The effective surface brightness ($\langle \mu_e \rangle$) is derived via $\langle \mu_e \rangle = m + 2.5 \log(2\pi R_e^2)$. Additionally, each surface brightness was corrected for the effects of surface brightness dimming and Galactic extinction, and also K-corrected for the effect of redshift on the broadband magnitudes (Campbell 2009).

It is most natural to have all FP parameters in logarithmic

units, so surface brightness values were converted from magnitude units (i.e. $\langle \mu_e \rangle$ in mag arcsec^{-2}) to log-luminosity units (i.e. $\log \langle I_e \rangle$ in $L_\odot$ pc^{-2}) using

$$\log \langle I_e \rangle = 0.4 M_\odot - 0.4 \langle \mu_e \rangle + 8.629 \, , \qquad (12)$$

where the absolute magnitude of the Sun, $M_\odot$, depends on the passband. For the J band, $M_\odot$=3.67; for the H band, $M_\odot$=3.33; and for the K band, $M_\odot$=3.29.[1] The value used for the magnitude of the Sun does not impact the fit, however, as it is simply a constant offset that is applied to the surface brightness.

Finally, the FP sample with both spectroscopic measurements from 6dFGS and photometric measurements from 2MASS in three J, H and K bands contains 11287 early-type galaxies in total. In Figure 4 we show the 6dFGSv redshift distribution (red), which is truncated at $cz_{max} = 16120$ km s^{-1} (a limit we apply as described in Section 3.2). This maximum redshift is approximately at the median redshift of the full 6dFGS redshift sample (grey); the 6dFGSv galaxies are sampled across this entire redshift range.

3.2 Selection Function

In our FP analysis there are selection limits imposed on or inherent in the sample that the fitting model must incorporate to provide accurate FP coefficients. In §2.5, we explained how these limits are included in our model, and now we provide the specific details of the selection criteria for the 6dFGSv data, as summarised in Table 1.

The 6dFGS FP sample of 11287 galaxies (Campbell 2009) has a velocity dispersion limit ($s \geqslant 2.05$) that is set by the instrumental resolution of the V band 6dFGS spectra. This limit is only achieved for galaxies with observed redshifts $cz < 16500$ km s^{-1}, since at higher redshifts crucial spectral features such as Fe 5270Å, Mg b 5174Å and Hβ 4861Å begin to move out of the V band spectra and into the lower resolution R band spectra. For the 6dFGS peculiar velocity sample we in fact impose a stricter upper redshift limit of $cz \leqslant cz_{max} = 16120$ km s^{-1} in the CMB frame in order to avoid an asymmetry on the sky when redshifts are converted from the heliocentric frame to the CMB frame (which we use for the peculiar velocities). This upper redshift limit for the sample excludes 750 galaxies.

We also only include galaxies with CMB-frame redshifts high enough ($cz \geqslant cz_{min} = 3000$ km s^{-1}) that their peculiar velocities are not significant relative to their recession velocities and so do not appreciably increase the scatter about the FP. This removes a further 92 low-redshift galaxies from the sample. However, unlike other selection criteria, galaxies excluded from the FP fitting by these upper and lower redshift limits are re-instated in the sample when deriving distances and peculiar velocities.

The morphologies and spectra of all the galaxies in the FP sample were classified by eye, as described in Section 3.5. Based on this visual inspection, 429 galaxies were removed on the basis of their morphological type, contamination of their fibre spectrum by a disk component, the (real or apparent) merger of their image with stars or other galaxies, or discernible emission line features in their spectra.

Our sample has slightly brighter flux limits than the original 6dFGS magnitude limits (Jones et al. 2009), reflecting the changes in the 2MASS (and, consequently, 6dFGS) magnitude limits that
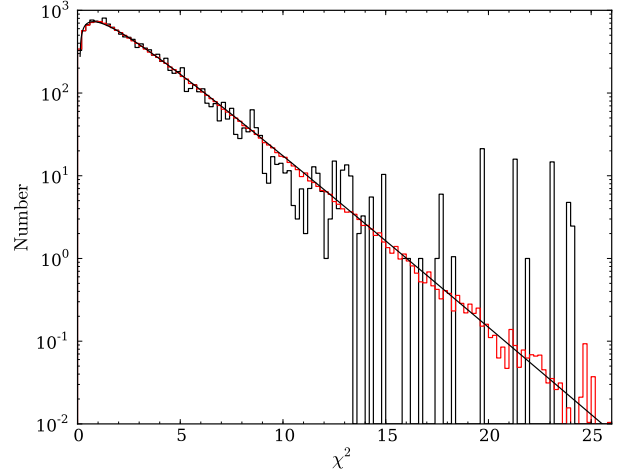
Figure 5. The distribution of χ^2 for the galaxies in the observed J band FP sample (black) and for mock galaxies in a sample drawn from the best-fitting 3D Gaussian model (red). The smooth curve is an analytic χ^2 distribution with 2.65 degrees of freedom, derived by fitting to the mock sample (there are fewer than 3 degrees of freedom due to the censoring of the 3D Gaussian by selection effects).

occurred after the 6dFGS sample was selected. To maintain high completeness in each passband over the whole sample area, we impose magnitude limits of $J \leqslant 13.65$, $H \leqslant 12.85$ and $K \leqslant 12.55$. At fixed luminosity distance, the magnitude limit is a strict cut in the r–i plane; given the distance range of the sample, this flux limit translates into a graduated selection effect in the r–i plane. In fitting the FP distribution we can account for the galaxies excluded by this selection effect by weighting the likelihood of each galaxy with a selection probability as described in §2.5.

Finally, in order to reduce the impact on the fit from a small number of galaxies with extremely low selection probabilities, we impose a minimum selection probability requirement ($S \geqslant 0.05$; see equation 10). We also remove outliers and blunders by requiring $\chi^2 \leqslant 12$. This χ^2 limit was derived empirically by comparing the χ^2 distributions for the observed galaxies and for mock galaxies drawn from the best-fitting 3D Gaussian model, as illustrated in Figure 5 for the J band sample (the H and K band samples are very similar). The number of observed galaxies at a given χ^2 begins to exceed the number of mock galaxies for $\chi^2 > 12$, which we attribute to outliers or blunders. The J, H and K samples have 48, 45 and 46 galaxies respectively above this limit (see Table 1), so we are typically removing just 0.5% of each sample.

The selection probability requirement is the only sample selection criterion that induces a significant residual bias, because it is the only one not accounted for in the normalisation of the probability distribution when computing the likelihood. We therefore correct for the (small) residual biases it produces by calibrating its impact using mock FP samples, as described in §4.1.

After applying all these selection criteria to obtain the samples to which we fit the FP, the numbers of galaxies remaining in each of the passbands are 8901 (J band), 8568 (H band) and 8573 (K band). The numbers of galaxies for which we can derive peculiar velocities are somewhat larger, since we can reinstate at least the galaxies excluded by the lower redshift limit.

Table 1. Summary of the 6dFGS Fundamental Plane sample selection criteria. The criteria apply to central velocity dispersion s, redshift distance cz (upper and lower limits), morphology, apparent magnitude m, selection probability S, and χ^2. The column N_{exc} shows the number of galaxies that would be removed by the specified selection cut *alone*. However, the number in brackets for each subtotal (or total) is the actual number of galaxies excluded when multiple selection limits are *combined* (i.e. without double-counting the galaxies that are eliminated by more than one selection criterion).

Sample	Selection Limit	N_g	N_{exc}	Comments
6dFGSz		124646		full redshift sample (with good quality z)
6dFGS$_{FP}$		11287		galaxies with derived FP parameters
6dFGSv	$s \geqslant 2.05$		287	aperture-corrected s cut
	$cz \geqslant 3000^*$		92	lower cz limit
	$cz \leqslant 16120^*$		750	upper cz limit
	Morphology		429	flagged classification (§3.5)
	SUBTOTAL:	9794	1558 (1493)	
6dFGSv$_J$	$J \leqslant 13.65$		1024	
	$S \geqslant 0.05$		32	
	$\chi^2 \leqslant 12$		48	
	TOTAL:	8901	1104 (893)	J band FP sample
6dFGSv$_H$	$m \leqslant 12.85$		1427	
	$S \geqslant 0.05$		41	
	$\chi^2 \leqslant 12$		45	
	TOTAL:	8568	1513 (1226)	H band FP sample
6dFGSv$_K$	$m \leqslant 12.55$		1398	
	$S \geqslant 0.05$		32	
	$\chi^2 \leqslant 12$		46	
	TOTAL:	8573	1476 (1221)	K band FP sample

*Note: these galaxies are excluded from the fitting of the FP, but are included when deriving FP distances and peculiar velocities.

3.3 Measurement Uncertainties

Each galaxy in the FP sample has an associated uncertainty from the measurement errors in each of its FP observables: size, velocity dispersion and surface brightness. The treatment of these errors is often simplified or approximated when fitting the FP—e.g. La Barbera et al. (2010a) use mock galaxy samples to approximate errors and correlations. However the maximum likelihood method allows us to to deal with the errors in all the observables (and their correlations) in a straightforward manner (see §2.3). For galaxy n, the measurement uncertainties are included through the error matrix, $\mathbf{E}_n$, given by

$$\mathbf{E}_n = \begin{pmatrix} \epsilon_{r_n}^2 + \epsilon_{rp_n}^2 & 0 & \rho_{ri}\epsilon_{r_n}\epsilon_{i_n} \\ 0 & \epsilon_{s_n}^2 & 0 \\ \rho_{ri}\epsilon_{r_n}\epsilon_{i_n} & 0 & \epsilon_{i_n}^2 \end{pmatrix} \quad (13)$$

The quantities ϵ_r, ϵ_s and ϵ_i are the observational errors on the FP parameters r, s and i, and their estimation is discussed in Campbell (2009).

The errors in the velocity dispersions, ϵ_s, are based on the Tonry & Davis (1979) formula derived for the Fourier cross-correlation technique, and are dependent on the measured signal-to-noise in the cross-correlation peak. These error estimates are validated by the large number of repeat velocity dispersion measurements in the 6dFGS sample. The typical error on the velocity dispersions in the 6dFGS FP sample is around 0.054 dex or 12%.

The photometric errors, ϵ_r and ϵ_i, were estimated by studying the scatter when comparing the sizes and surface brightnesses obtained from the three independent 2MASS passbands. We assume that the surface brightness colours (i.e. the values of $i_j - i_h$, $i_j - i_k$, and $i_h - i_k$) are very similar for every galaxy within each narrow range of apparent magnitude, and that the dominant cause

of variation from one galaxy to the next is the error in the surface brightness measurements. We then compute the mean square deviation in surface brightness colour for the J and H bands, δ_{jh}^2, over the N galaxies within a specified apparent magnitude bin, given by

$$\delta_{jh}^2 = (\Sigma_{n=1,N}[(i_{j,n} - i_{h,n}) - < i_j - i_h >]^2)/N . \quad (14)$$

If we assume that δ_{jh}^2 is the sum of the mean square errors in i_j and i_h, and that δ_{jk}^2 and δ_{hk}^2 are likewise the sum of the mean square errors in i_j and i_h, and i_h and i_k, respectively, then we can solve for the error in i_j alone, obtaining

$$\epsilon_{i,j} = [0.5(\delta_{jh}^2 + \delta_{jk}^2 - \delta_{hk}^2)]^{1/2} . \quad (15)$$

This is the error on i_j, which we compute separately in apparent magnitude bins of width 0.2 mag. We similarly compute $\epsilon_{i,h}$ and $\epsilon_{i,k}$, shifting the magnitude bins by the mean colour of the galaxies in the sample, to get the surface brightness errors in each band as a function of apparent magnitude.

Figure 6 shows the J, H, and K band surface brightness errors as a function of J, H, and K apparent magnitude. We approximate the errors using the following relations, which are shown as dashed lines in Figure 6:

$$\epsilon_i = \begin{cases} 0.024\,m_J - 0.232 & m_J \geqslant 11.7 \\ 0.048 & m_J < 11.7 \end{cases}$$

$$\epsilon_i = \begin{cases} 0.028\,m_H - 0.248 & m_H \geqslant 10.6 \\ 0.048 & m_H < 10.6 \end{cases} \quad (16)$$

$$\epsilon_i = \begin{cases} 0.040\,m_K - 0.352 & m_K \geqslant 10.3 \\ 0.060 & m_K < 10.3 . \end{cases}$$

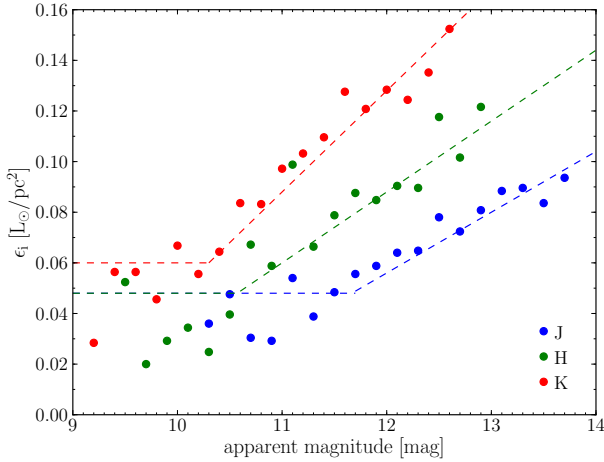Note that at bright apparent magnitudes we conservatively truncate

Figure 6. The blue (green, red) points show the derived measurement error on i_j (i_h, i_k) as a function of m_J (m_H, m_K). The measurement errors, ϵ_i, are in units of $\log[\mathrm{L}_\odot\,\mathrm{pc}^{-2}]$. We approximate these measurement error relations by the dashed lines of the corresponding colours, which are specified by equation 16).

the J and H band errors at 0.048 mag and the K band error at 0.060 mag.

There is no correlation between the errors in s and those in r or i, but there is a strong correlation between those in r and i. This is quantified by a correlation coefficient that is determined empirically by studying the distribution of the differences in r against the differences in i for pairs of independent passbands. The coefficient is found to be $\rho_{ri} = -0.95$ for all passbands. To preserve this correlation, the error in r is calculated directly from the error in i using $\epsilon_r = 0.68\epsilon_i$. For the J band, the typical error in the effective radius is around 0.049 dex (11%) and in surface brightness is around 0.073 dex (17%). However in the correlated combination in which these quantities appear in the FP, namely $X_{\mathrm{FP}} = r - bi$, the typical error in X_{FP} is just 0.016 dex (4%).

There is an additional error term for effective radius, ϵ_{rp}, which allows for the uncertainty in the conversion of angular to physical units under the assumption that the galaxy is at its redshift distance (i.e. neglecting the unknown peculiar velocity). This error term is approximated as $\epsilon_{rp_n} = \log(1 + 300\,\mathrm{km\,s}^{-1}/cz_n)$, which assumes a typical peculiar velocity of $300\,\mathrm{km\,s}^{-1}$ for the galaxies in the sample (Strauss & Willick 1995). Because we explicitly exclude from the sample galaxies at low redshifts, where the peculiar velocities are potentially large relative to the recession velocities (see §3.2), ϵ_{rp} is typically <3% and contributes less than 10% to the overall error in r.

We note that a similar error on surface brightness exists due to the use of observed redshifts (uncorrected for peculiar velocities) in computing the cosmological dimming. However, we do not include this in our measurement error matrix because it is typically less than 0.4%, which is negligible when added in quadrature to the photometric measurement errors.

3.4   Group Catalogue

Groups and clusters in the the 6dFGS sample were identified using a friends-of-friends group-finding algorithm (Merson et al., in prep.). The algorithm follows a similar procedure to the group-finding method used to construct the 2dF Percolation-Inferred Galaxy Groups (2PIGG) Catalogue of the 2dF Galaxy Redshift

Survey (Eke et al. 2004), but it is re-calibrated to the specifications (redshift depth and sample density) of the 6dFGS.

This group catalogue is used to test the universality of the Fundamental Plane (i.e. whether the FP coefficients vary with galaxy environment) and to derive mean redshifts for groups and thus group distances and peculiar velocities (in addition to distances and peculiar velocities for single galaxies). Combining galaxies into groups is important to our future peculiar velocity analysis for two reasons: (i) it minimises the 'Finger-of-God' distortions of distances and peculiar velocities produced by virialised structures in redshift space; (ii) it allows us to correct any variations in the FP with environment that might bias the distance and peculiar velocity estimates.

From the initial 11287 galaxies in the 6dFGS FP subsample, there were 3186 galaxies found in groups containing at least four members (and so deemed to have reliable group membership status). The flux-limited nature of our survey meant that the faintest members of a group might not have been observed, so the richness of a group (which we use as proxy for global environment) is defined as the number, N_R, of observed galaxies in the group brighter than a specified absolute magnitude, chosen so that galaxies brighter than this would be visible throughout the sample volume. Any galaxy not in a group was given a richness $N_R=0$, signifying its status as either a field galaxy or a bright member of a poor group.

In addition to this group catalogue, we also determine parameters that define each galaxy's local environment using the method described in Wijesinghe et al. (submitted, 2012).

In this catalogue, local environment is represented by the projected comoving distance, d_5 (in Mpc) to the 5th nearest neighbour and the surface density, Σ_5 (in galaxies Mpc^{-2}), is therefore defined as $\Sigma_5 = 5/\pi * d_5^2$. To exclude contamination from foreground and background galaxies these density measurements are made within a velocity cylinder of $\pm 1000\,\mathrm{km\,s}^{-1}$. In our final FP sample, there are 8258 galaxies for which we can calculate reliable values of these estimators of local environment

3.5   Morphological Classification

All 11287 galaxies in the 6dFGS FP sample were visually inspected to provide morphological classifications. Each galaxy was examined by up to four experienced observers, and on average classified twice. This was done to determine and flag any galaxies without dominant bulges that might bias, or add scatter to, the FP fits, and also to allow us to test whether ellipticals, lenticulars and spiral bulges have different FP distributions.

All of the galaxies were visually inspected using the 2MASS J, H and K band images and also the higher-resolution Super-COSMOS images in the b_J and r_F bands. The galaxies were classified into the standard morphological types: elliptical (E), lenticular (S0), spiral (Sp) and irregular or amorphous (Irr), plus the transition cases E/S0, S0/Sp and Sp/Irr. The presence of dust lanes was also flagged. The galaxy images had 6.7 arcsec diameter circles superimposed in order to determine whether the 6dF fibre enclosed only bulge light or whether there was significant contamination by light from the disks of S0 and Sp galaxies. At the same time, the 6dFGS spectra were scrutinised for any discernible emission features.

From this sample there were 429 galaxies excluded on the basis of one or more of the criteria defined below. If any one of these criteria was flagged by two or more classifiers, or flagged by the single classifier in cases where a galaxy was only classified once, then the galaxy was excluded as not being bulge-dominated

or as problematic in some other respect. The exclusion criteria were: (i) galaxy morphology classified as irregular or amorphous; (ii) galaxy identified as edge-on with a full dust lane; (iii) significant fraction of light in fibre is from a disk; and (iv) light in fibre contaminated by nearby star, galaxy or defect.

4 MOCK GALAXY FP SAMPLES

We now describe the process of generating mock catalogues from a model that reproduces all of the main features of the observed data sample as closely as possible. It is important that the mock samples are robust and well calibrated, as they serve several functions. We use them: to perform comparisons of different fitting methods (§2.2); to validate the ML fitting method and the assumption of a 3D Gaussian model for the data (§4.1 and §5.3); to correct for residual bias effects (§4.2); and to determine the accuracy and precision of the fits (§5.2).

4.1 Mock Sample Algorithm

We create mock samples from a given set of FP parameters $\{a, b, c, \bar{r}, \bar{s}, \bar{i}, \sigma_1, \sigma_2, \sigma_3\}$ using the following steps to generate each mock galaxy:

(i) Draw values for v_1, v_2 and v_3 at random from a 3D Gaussian with corresponding specified variances σ_1, σ_2 and σ_3.

(ii) Transform these values from the $\mathbf{v}$-space (principal axes) coordinate system to the $\{\mathbf{r}, \mathbf{s}, \mathbf{i}\}$-space (observed parameters) coordinate system using the inverse of the relations in equation 5 with the specified FP slopes (a and b) and FP mean values ($\bar{r}$, $\bar{s}$ and $\bar{i}$).

(iii) Generate a comoving distance from a random uniform density distribution over the volume out to $cz_{max} = 16120\,\mathrm{km\,s^{-1}}$ using the assumed cosmology. This comoving distance is converted to an angular diameter distance in order to calculate an angular effective radius from a physical effective radius.

(iv) The redshift of each mock galaxy is also derived from this comoving distance; it must be greater than the lower limit on cz to remain in the mock sample.

(v) Derive an apparent magnitude from the surface brightness and effective radius (in angular units) of each galaxy, obtained at step (ii), using $m = \langle\mu_e\rangle - 2.5\log[2\pi(R_e^\theta)^2]$.

(vi) Estimate rms measurement uncertainties from this magnitude via the prescription given in §3.3, and use these uncertainties to generate Gaussian measurement errors in $\{r, s, i\}$ from the error matrix in equation 13 (including the correlation between ϵ_r and ϵ_i).

(vii) Add these measurement errors to $\{r, s, i\}$ to obtain the observed values of the FP parameters; the velocity dispersion must be greater than the lower selection limit to remain in the mock sample.

(viii) Compute the observed magnitude using the observed values of r and i (i.e. including measurement errors); it must be brighter than the limiting magnitude for the galaxy to remain in the sample.

(ix) Compute the selection probability from the observed magnitude and redshift using equations 9 and 10; it must be greater than the minimum selection probability for the galaxy to remain in the mock sample.

This process is repeated until the desired number of galaxies is generated for the mock sample.

Figure 7 compares the distributions of effective radius, velocity dispersion and surface brightness for the 6dFGS J band sample and a mock sample generated from the best-fitting 3D Gaus-

Table 2. Bias corrections for each of the FP parameters. These corrections are added to the fitted parameters to remove the residual bias. Note that these corrections are small for all parameters.

a	b	c	$\bar{r}$	$\bar{s}$	$\bar{i}$	σ_1	σ_2	σ_3
0.022	-0.008	-0.027	-0.006	-0.001	0.004	0.0002	0.0026	0.0013

sian model (see below) having the same number of galaxies, the same selection criteria and the same observational errors. The mock sample accurately replicates the distributions of the galaxies in FP space, both for the observed parameters (r, s and i) and the 'natural' parameters (v_1, v_2 and v_3), which are shown in Figure 8. This close match between the model and the data justifies our use of a 3D Gaussian model for the distribution of galaxies in FP space.

4.2 Residual Bias Corrections

The only effect that is not explicitly corrected for in the maximum likelihood fitting process, and which introduces a (small) bias, is the exclusion of low-selection-probability (i.e. high-weight) galaxies. These galaxies are excluded because: (a) they may be outliers; and (b) they enter the likelihood with high weights and may therefore distort the fits. They cannot be directly accounted for in the ML fit because we do not have an explicit model for the distribution of outliers.

In practice this bias is small because only a small number of galaxies are excluded, and may be quantified under the assumptions of our model using mock samples. By applying the same selection criteria to the mocks as we do to the data, we can recover the correction Δy for the residual bias in some parameter y as the difference between the value y_{obs} obtained from fitting the observed data and the value y_{mock} recovered as the average from ML fits to many mock samples:

$$\Delta y = y_{\mathrm{obs}} - y_{\mathrm{mock}} \qquad (17)$$

where y can be any of the parameters describing the 3D Gaussian model, $\{a, b, c, \bar{r}, \bar{s}, \bar{i}, \sigma_1, \sigma_2, \sigma_3\}$. To correct fits to the observed data for residual bias, these corrections should be added to the best-fit FP parameter values to recover the 'true' parameters:

$$y_{\mathrm{cor}} = y_{\mathrm{obs}} + \Delta y \,. \qquad (18)$$

These corrections were obtained for mock samples of increasing sample size, with N_g ranging from 1000 to 10000 galaxies. For all parameters the bias correction was found to be constant for all sample sizes. We have therefore employed a fixed bias correction for each parameter regardless of sample size. These corrections are listed for each fitted FP parameter in Table 2.

5 THE FUNDAMENTAL PLANE

5.1 The 3D Fundamental Plane

Fundamental Plane studies in optical passbands are relatively abundant, while studies in near-infrared passbands are less so. It is only recently that large, homogeneous FP data sets across both optical and near-infrared wavelengths have become available (Hyde & Bernardi 2009; La Barbera et al. 2010b). Using near-infrared photometry in FP analyses is advantageous because in these passbands
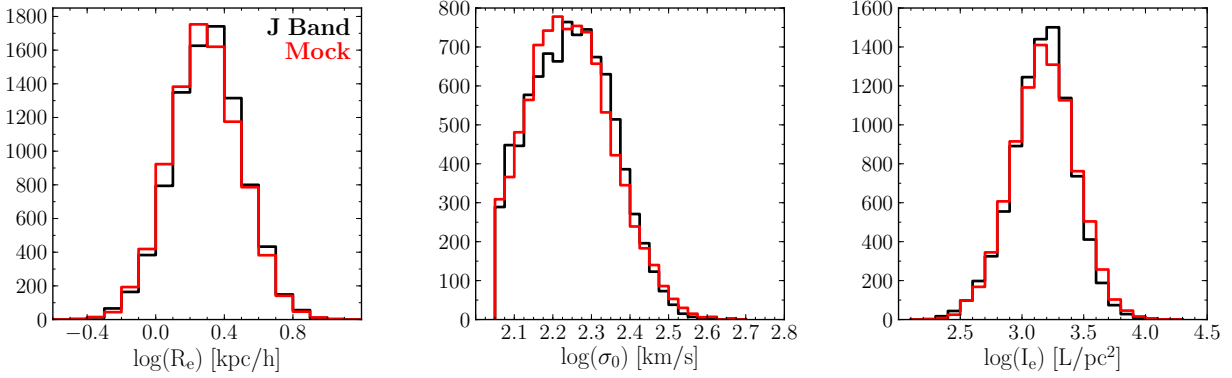
Figure 7. The distribution of the observed Fundamental Plane parameters $\log R_e$, $\log \sigma_0$ and $\log \langle I_e \rangle$ for the 6dFGS J band sample (black) and a mock sample (red) of the same size ($N_g = 8901$) and the same selection criteria, with FP coefficients $a = 1.52$ and $b = -0.89$.
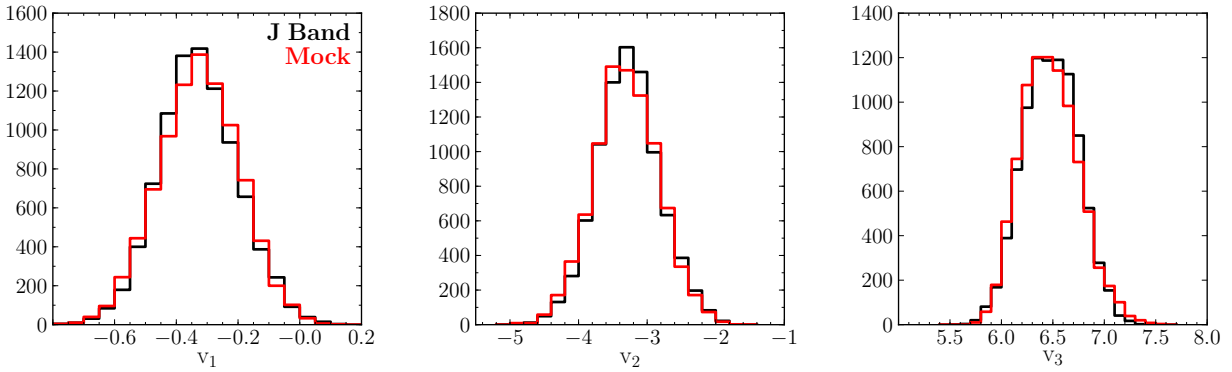

Figure 8. The distribution of the natural Fundamental Plane parameters v_1, v_2 and v_3 for the 6dFGS J band sample (black) and a mock sample (red) of the same size ($N_g = 8901$) and the same selection criteria, with FP coefficients $a = 1.52$ and $b = -0.89$.

the lower extinction reduces the variations due to dust and the dominance of older stellar populations reduces the variations due to recent star-formation (at least in the absence of a significant population of intermediate-age AGB stars—cf. Maraston 2005). Comparison of optical and near-infrared observations can reveal the effect of variations in the mass-to-light (M/L) ratios on the Fundamental Plane.

Figure 9 is a 3D visualisation of the 6dFGS J band FP sample that can be interactively viewed in the full 3D space of the observed parameters r, s and i. This figure (like Figure 3) was created with the S2PLOT programming library. It is important to show the 3D view of the FP, rather than the 2D plots usually found in the literature, because information is lost in projecting the FP onto two dimensions from its native three dimensions, and the true properties of the 3D distribution of the FP are disguised. Figure 9 reveals in 3D the well-known features of the FP, including the small scatter in the edge-on view relative to the other two dimensions, and the Gaussian nature of the distribution in all three dimensions; the impact of sampling effects, such as the hard selection limit in velocity dispersion, are also readily apparent.

5.2 Fundamental Plane parameters and uncertainties

Using our maximum likelihood fitting routine we recover the best-fit FP in the J, H and K passbands for samples containing 8901, 8568 and 8573 galaxies respectively. The full details of the FP fits in these bands are given in Table 3, including all eight fitted parameters together with the constant of the fit (c), the offset of the plane

in the r-direction (r_0; see below), the total rms scatter about the FP in the r-direction (σ_r), and the total rms scatter in distance (σ_d); the difference between these two scatters is discussed in §8.

The errors in the best-fit FP parameters that are given in Table 3 are estimated as the rms scatter in fits to multiple mock samples generated as described in §4 using the parameters of the best-fit FP. The distribution of the parameters derived from ML fits to 1000 mock samples (each sample containing 8901 galaxies, as for the 6dFGS J band sample) are shown in Figure 10. Note that the residual bias corrections (the differences between the input parameters and the mean of the fitted parameters) are comparable to or less than the rms scatter in the fits (i.e. comparable to or less than the random errors in the fitted values). This highlights the accuracy with which the ML method recovers the FP parameters even in the presence of significant observational errors and various types of sample censoring.

Both the bias corrections and the random errors are small; the fractional errors in the FP slopes (a and b) and dispersions (σ_1, σ_2 and σ_3) are all less than 2%. For the offset of the FP, $c \equiv \bar{r} - a\bar{s} - b\bar{i}$, the uncertainty is 0.054 dex or 12%. However as a measure of the uncertainty in the relative sizes and distances of galaxies due to the fit this 'intercept' offset is misleading. A better measure is the uncertainty in $\bar{r}$, which is 0.9%; but even this is an over-estimate of the practical impact of the uncertainty in the fit, as the point ($\bar{r}, \bar{s}, \bar{i}$) is at the edge of the observed distribution (i.e. the observed distribution is well-fitted by a Gaussian centred close to the velocity dispersion limit). The most realistic estimate of the uncertainty in the r-axis offset of the fitted FP, as it affects size and
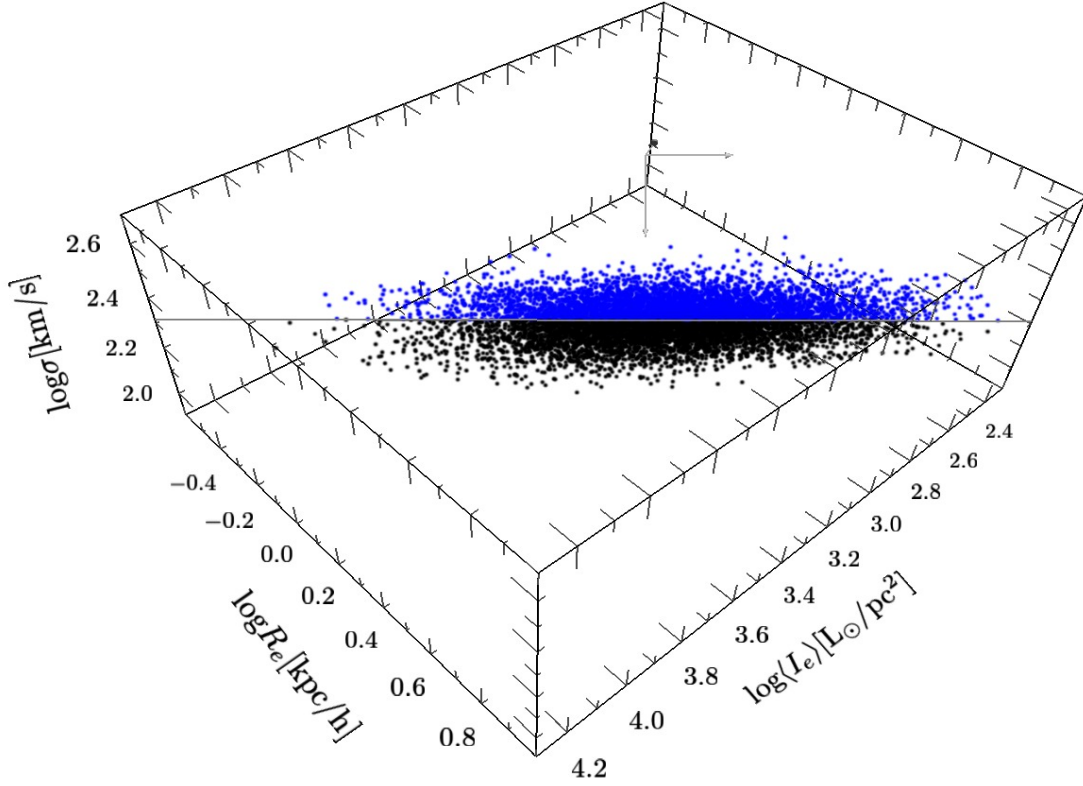
Figure 9. Interactive 3D visualisation of the 6dFGS J band Fundamental Plane in $\mathbf{r}, \mathbf{s}, \mathbf{i}$ space. The best fitting plane (in grey) has slopes $a = 1.523$ and $b = -0.885$, and an offset $c = -0.330$. The galaxies are colour-coded according to whether they are above (blue) or below (black) the best-fit plane. The 1σ, 2σ, and 3σ contours of the 3D Gaussian distribution (light grey) can be toggled in the interactive plot environment. (Readers using Acrobat Reader v8.0 or higher can enable interactive 3D viewing of this schematic by mouse clicking on the figure; see Appendix B for more detailed usage instructions.)

Table 3. Best-fit 6dFGS FP parameters (including bias corrections) and their associated uncertainties for: (i) the full J, H and K samples; (ii) the J band N_R richness subsamples (field, low, medium and high); (iii) the J band Σ_5 local environment subsamples (low, medium and high); and (iv) the J band morphology subsamples (early and late types). As well as the nine FP parameters, the table also lists: N_g, the number of galaxies in each sample; r_0, the location of the FP at the fiducial point $(s_0 = 2.3, i_0 = 3.2)$; σ_r, the scatter about the FP in the r-direction (see §8.2); and σ_d, the scatter in the distance (see §8.3).

Sample	N_g	a	b	c	$\bar{r}$	$\bar{s}$	$\bar{i}$	r_0	σ_1	σ_2	σ_3	σ_r	σ_d
J band	8901	1.523±0.026	-0.885±0.008	-0.330±0.054	0.184±0.004	2.188±0.004	3.188±0.004	0.345±0.002	0.053±0.001	0.318±0.004	0.170±0.003	0.127 (29.7%)	0.097 (22.5%)
H band	8568	1.473±0.024	-0.876±0.008	-0.121±0.051	0.175±0.004	2.190±0.003	3.347±0.004	0.465±0.002	0.051±0.001	0.318±0.004	0.167±0.003	0.123 (28.8%)	0.096 (22.3%)
K band	8573	1.459±0.024	-0.858±0.008	-0.103±0.050	0.153±0.005	2.189±0.003	3.430±0.005	0.511±0.003	0.050±0.001	0.329±0.004	0.166±0.003	0.123 (28.8%)	0.095 (22.1%)
$N_R \leqslant 1$	6495	1.512±0.030	-0.882±0.010	-0.307±0.063	0.183±0.005	2.187±0.004	3.197±0.005	0.351±0.002	0.053±0.001	0.315±0.005	0.161±0.003	0.127 (29.7%)	0.097 (22.5%)
$2 \leqslant N_R \leqslant 5$	1248	1.582±0.058	-0.899±0.021	-0.436±0.122	0.154±0.014	2.170±0.012	3.168±0.012	0.331±0.005	0.051±0.002	0.324±0.011	0.201±0.009	0.126 (29.3%)	0.098 (22.7%)
$6 \leqslant N_R \leqslant 9$	546	1.573±0.088	-0.862±0.029	-0.538±0.187	0.220±0.017	2.208±0.012	3.154±0.015	0.327±0.006	0.044±0.003	0.325±0.014	0.181±0.011	0.120 (28.0%)	0.094 (21.8%)
$N_R \geqslant 10$	612	1.504±0.094	-0.903±0.029	-0.248±0.195	0.228±0.016	2.220±0.012	3.171±0.014	0.324±0.006	0.054±0.003	0.316±0.013	0.173±0.011	0.129 (30.1%)	0.095 (22.1%)
$\Sigma_5 \leqslant 0.07$	2664	1.486±0.051	-0.848±0.014	-0.354±0.113	0.190±0.008	2.192±0.005	3.203±0.006	0.354±0.004	0.053±0.002	0.314±0.007	0.147±0.006	0.126 (29.3%)	0.095 (21.9%)
$0.07 < \Sigma_5 \leqslant 0.25$	2812	1.516±0.043	-0.915±0.015	-0.220±0.090	0.175±0.008	2.183±0.007	3.189±0.007	0.343±0.003	0.053±0.002	0.313±0.007	0.173±0.006	0.126 (29.5%)	0.097 (22.5%)
$\Sigma_5 > 0.25$	2782	1.564±0.039	-0.889±0.013	-0.418±0.079	0.188±0.009	2.190±0.007	3.170±0.008	0.335±0.003	0.050±0.001	0.326±0.007	0.185±0.006	0.127 (29.6%)	0.097 (22.5%)
E+E/S0+S0	6956	1.535±0.029	-0.879±0.010	-0.384±0.060	0.156±0.005	2.199±0.004	3.230±0.004	0.339±0.002	0.052±0.001	0.296±0.004	0.170±0.003	0.128 (29.8%)	0.096 (22.3%)
Sp bulges	1945	1.586±0.067	-0.861±0.017	-0.512±0.138	0.305±0.009	2.151±0.008	3.016±0.008	0.384±0.006	0.052±0.002	0.319±0.008	0.157±0.005	0.127 (29.7%)	0.097 (22.6%)

distance estimates for 6dFGS galaxies, is given by the uncertainty in r_0, the r-value of the fitted FP at a fiducial point in the middle of the observed sample: $s_0 \equiv 2.3$ and $i_0 \equiv 3.2$. The rms scatter in $r_0 \equiv as_0 + bi_0 + c$ is just 0.5%.

5.3 Model validation

That our 3D Gaussian model is a good representation of the observed distribution of galaxies in FP space is verified by the remarkable similarities between the mock and data likelihoods. The histogram of log-likelihood values in Figure 11 gives the distribu-
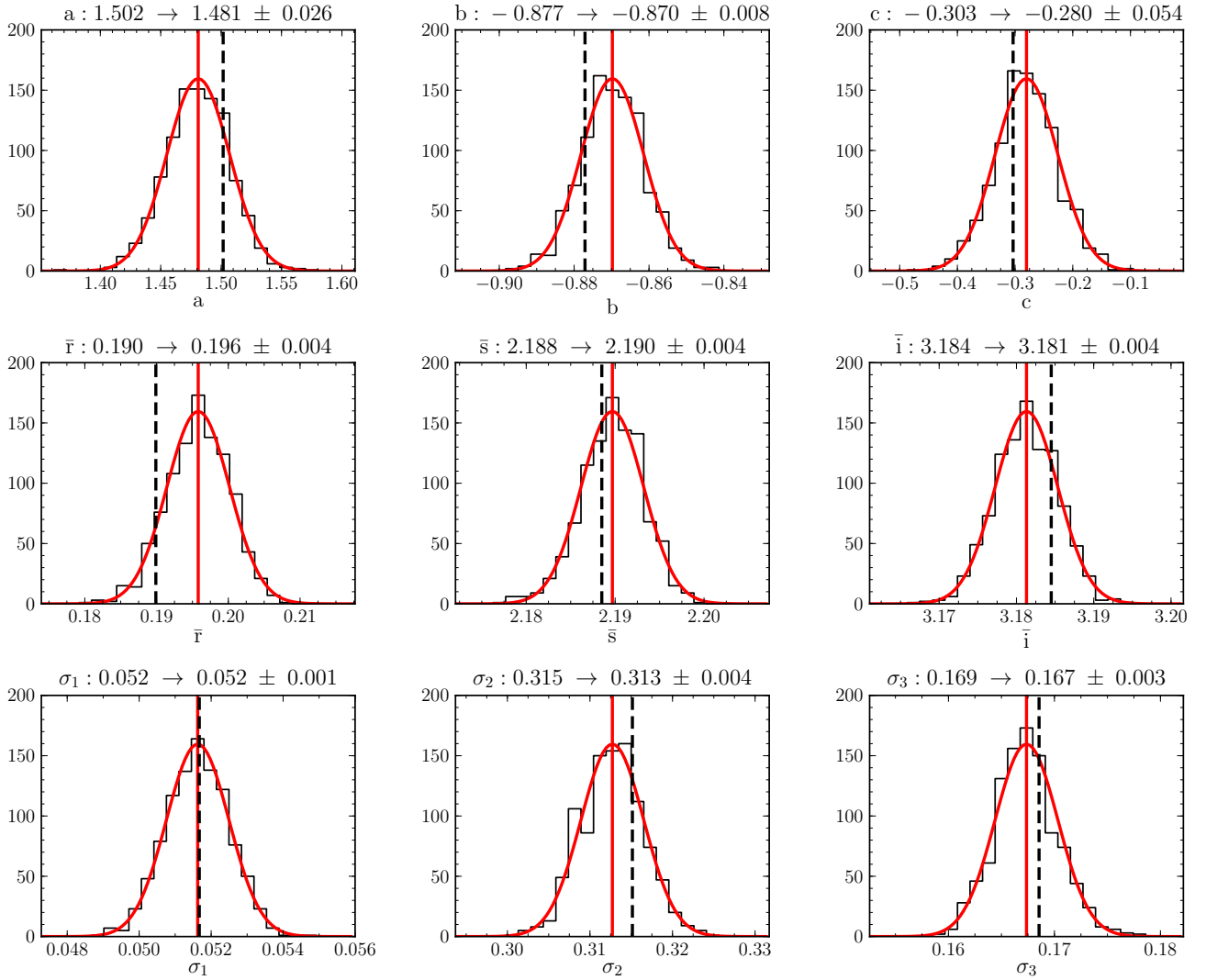
Figure 10. Histograms of the maximum-likelihood best-fit values of the J band FP parameters $\{a,b,c,\bar{r},\bar{s},\bar{i},\sigma_1,\sigma_2,\sigma_3\}$ from 1000 simulations. Each panel is labelled at the top with the name of the parameter, the input value of the parameter for the 1000 mock samples, and the mean and rms of the best-fit parameters obtained from ML fits to these mocks; a Gaussian with this mean and rms is overplotted on the histograms. The vertical dashed line shows the input value of the parameter and the vertical solid line shows the mean of the best-fit values. The residual bias correction (see §4.2) is the offset between the dashed line and the solid line; in all cases this is comparable to or smaller than the modest rms scatter in the fitted parameter.

tion from the same 1000 mock simulations as Figure 10, derived in two ways: first by calculating the likelihoods for all the mocks using the best-fit FP of the data (red histogram), and second, by calculating the likelihoods using the best-fit FP values from each individual mock (black histogram). It makes little difference which method is used, as the distribution of likelihoods for these two situations are very similar.

The mean of each histogram (red: $\ln \mathcal{L} = 20878 \pm 225$; black: $\ln \mathcal{L} = 20897 \pm 224$) is plotted as a solid line. The likelihood of the best fit to the actual data ($\ln \mathcal{L} = 21126$) is shown by the dashed vertical line, and is larger than these means but still well within the range of likelihoods spanned by the mock samples. The fact that the likelihood recovered from the data is higher than that from the mocks (i.e. $\ln \mathcal{L}$ is more positive) is a result of excluding the χ^2 outliers from the data, which may also remove the extreme tail of the Gaussian distribution. Genuine outliers do not exist in the mock samples and so no χ^2 clipping is applied, and the lower likelihoods of the mock samples in Figure 11 reflect this difference.

In summary, the similarity in likelihood values indicates that the fitting algorithm has accurately recovered the input FP and also that the 3D Gaussian model is a suitable representation of the observed FP distribution.

5.4 Additional σ-component of 3D Gaussian vectors

Our 3D Gaussian model of the FP assumes that the s-component of the $\mathbf{v_2}$ vector is zero; i.e. that the vector representing the longest axis of the 3D Gaussian lies wholly in the r–i plane. This is based in part on previous studies (Saglia et al. 2001; Colless et al. 2001), and in part assumed for convenience and simplicity.

We can test how accurate this assumption is by extending the vector definitions of equation 5 to include this component, with
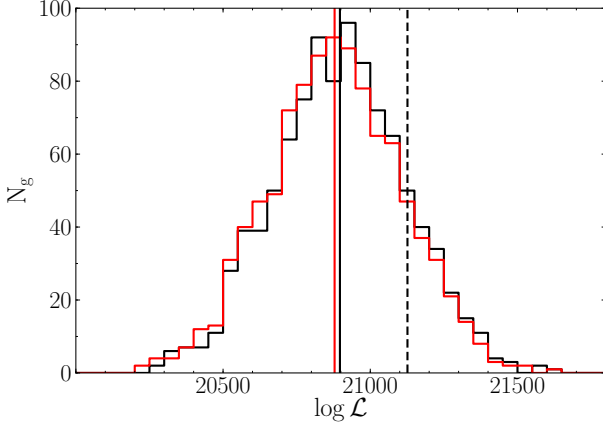
Figure 11. Distribution of likelihood values from 1000 mock samples. The FP coefficients used to generate these mock simulations are the same values used to generate the mocks in Figure 10. The likelihood values in the red histogram were calculated for each mock sample using these identical input FP values, whereas the likelihood values in the black histogram were calculated using the individual best fit for each mock. The mean likelihoods from these mocks (red: $\ln \mathcal{L} = 20878 \pm 225$; black: $\ln \mathcal{L} = 20897 \pm 224$) are indicated by the solid lines, and are comparable to but lower than the best-fit likelihood obtained for the actual data ($\ln \mathcal{L} = 21126$), shown by the dashed black line.

coefficient k, defining the set of orthogonal axes

$$\mathbf{v_1} = \hat{\mathbf{r}} - a\hat{\mathbf{s}} - b\hat{\mathbf{i}},$$
$$\mathbf{v_2} = \hat{\mathbf{r}} - k\hat{\mathbf{s}} + (1 - ka)\hat{\mathbf{i}}/b, \qquad (19)$$
$$\mathbf{v_3} = (ka^2 - a + kb^2)\hat{\mathbf{r}} + (ka - 1 - b^2)\hat{\mathbf{s}} + (kb + ab)\hat{\mathbf{i}}$$

and then including this extra parameter in our fitting algorithm. We then perform a nine-parameter maximum likelihood fit with the same J band FP sample of galaxies and find a best-fit value $k = 0.09 \pm 0.01$, and a J band FP given by

$$r = (1.51 \pm 0.03)s - (0.86 \pm 0.01)i - (0.39 \pm 0.06) . \quad (20)$$

Therefore, when there are no constraints placed on the components of $\mathbf{v_2}$, the s-component is close to—but slightly larger than—zero. The coefficient of s is much smaller than the coefficients of any of the other vector components, the intrinsic scatter about the plane ($\sigma_1 = 0.052$) is the same to within 0.5%, and the error in distances is 24.3% (i.e. slightly larger than for the standard 8-parameter model). Hence the addition of this ninth parameter provides no practical advantages, and we retain the simplifying approximation of fixing $k \equiv 0$.

5.5 Adding age to the Fundamental Plane model

Springob et al. (2012) found that there is a clear trend of galaxy age through the FP (i.e. along the $\mathbf{v_1}$ direction), as expected from models of the effect of stellar populations on mass-to-light ratios (e.g. Bruzual & Charlot 2003; Korn, Maraston & Thomas 2005). The variation of age through the FP is shown in Figure 12, a 3D plot of the FP-space distribution of the sub-sample of 6579 galaxies with stellar population parameters measured by Springob et al. (2012), with colour encoding $\log(\text{age})$. Here we investigate whether this trend in age can be incorporated into the FP model and used to reduce the overall scatter of the FP by exploring a very simple extension of the model that allows for a linear trend of age through the FP.

We include an age component in our existing FP model by adding $\log(\text{age})$ as a fourth dimension in FP space along with r, s, and i. We assume that age varies almost entirely in the $\mathbf{v_1}$ direction (normal to the plane), as suggested by the results of Springob et al. (2012). We therefore assume the $\mathbf{v_2}$ and $\mathbf{v_3}$ vectors have no age component, and derive a fourth v-space vector that is orthogonal to the other three vectors. The resulting vector definition of this new 4D Gaussian model is

$$\mathbf{v_1} = \hat{\mathbf{r}} - a\hat{\mathbf{s}} - b\hat{\mathbf{i}} - k_A\hat{\mathbf{A}},$$
$$\mathbf{v_2} = \hat{\mathbf{r}} + \hat{\mathbf{i}}/b,$$
$$\mathbf{v_3} = -\hat{\mathbf{r}}/b - (1 + b^2)\hat{\mathbf{s}}/(ab) + \hat{\mathbf{i}}$$
$$\mathbf{v_4} = \hat{\mathbf{r}} - a\hat{\mathbf{s}} - b\hat{\mathbf{i}} + (1 + a^2 + b^2)\hat{\mathbf{A}}/k_A \qquad (21)$$

where k_A is the component of $A = \log(\text{age})$ in the $\mathbf{v_1}$ direction. Additional parameters that need to be fitted along with k_A in this model are the mean of the 4D Gaussian in $\log(\text{age})$ ($\bar{A}$) and the intrinsic scatter in the $\mathbf{v_4}$ vector (σ_4); this gives a total of 11 free parameters to be fitted. Both the intrinsic variance matrix, $\mathbf{\Sigma}$, and the observed measurement error matrix, $\mathbf{E}$, are also extended to four dimensions to include σ_4 and age measurement errors, respectively.

The 4D Gaussian model including age is then fit to this sub-sample resulting in an FP given by

$$r = (1.56 \pm 0.03)s - (0.89 \pm 0.01)i - (0.13 \pm 0.01)A - 0.43 \pm 0.06 \qquad (22)$$

with $\sigma_1 = 0.048 \pm 0.001$ and $\sigma_4 = 0.40 \pm 0.01$. Although the intrinsic scatter through the FP (σ_1) is reduced from its value in the standard 3D Gaussian model (where $\sigma_1 = 0.053$), the large scatter in σ_4 and steeper slope in s suggest that the scatter in distance has not been reduced by including an age component. In fact, the scatter in distance (see §8.3) is slightly larger, at $\sigma_d = 0.010 \text{ dex}$ (23.3%), than for the standard 3D Gaussian model, where $\sigma_d = 0.097 \text{ dex}$ (22.5%).

We conclude that: (i) there is a statistically significant contribution from age variations to the scatter through the FP, which is slightly reduced by including age in the FP model; and (ii) the combination of large measurement errors on individual galaxy ages, intrinsic scatter in age about the FP, and the tilt of the FP (specifically, the angle between $\mathbf{v_1}$ and $\mathbf{r}$), means that—for the 6dFGS sample—including age does not improve the distance estimates obtained from the FP. This might change, however, if substantially more precise age measurements were available.

5.6 Bayesian model selection

To justify our choice of the standard 3D Gaussian model, as defined in §2, over the alternative models we have considered in §5.4 and §5.5, we compare these models using the Bayes information criterion (Schwarz 1978).

The Bayes information criterion, or BIC, can be used to choose between different models and determine whether increasing the number of free parameters in the model will result in overfitting. It has the advantages of being easy to compute and independent of the assumed priors for the models, and in the limit of large sample size it approaches $-2\ln(B)$, where B is the the Bayes factor that gives the relative posterior odds of the models under comparison. The BIC depends on the size of the sample (N), the log-likelihood of the best fit ($\ln \mathcal{L}$), and the number of free parameters in the model (k), and is given by

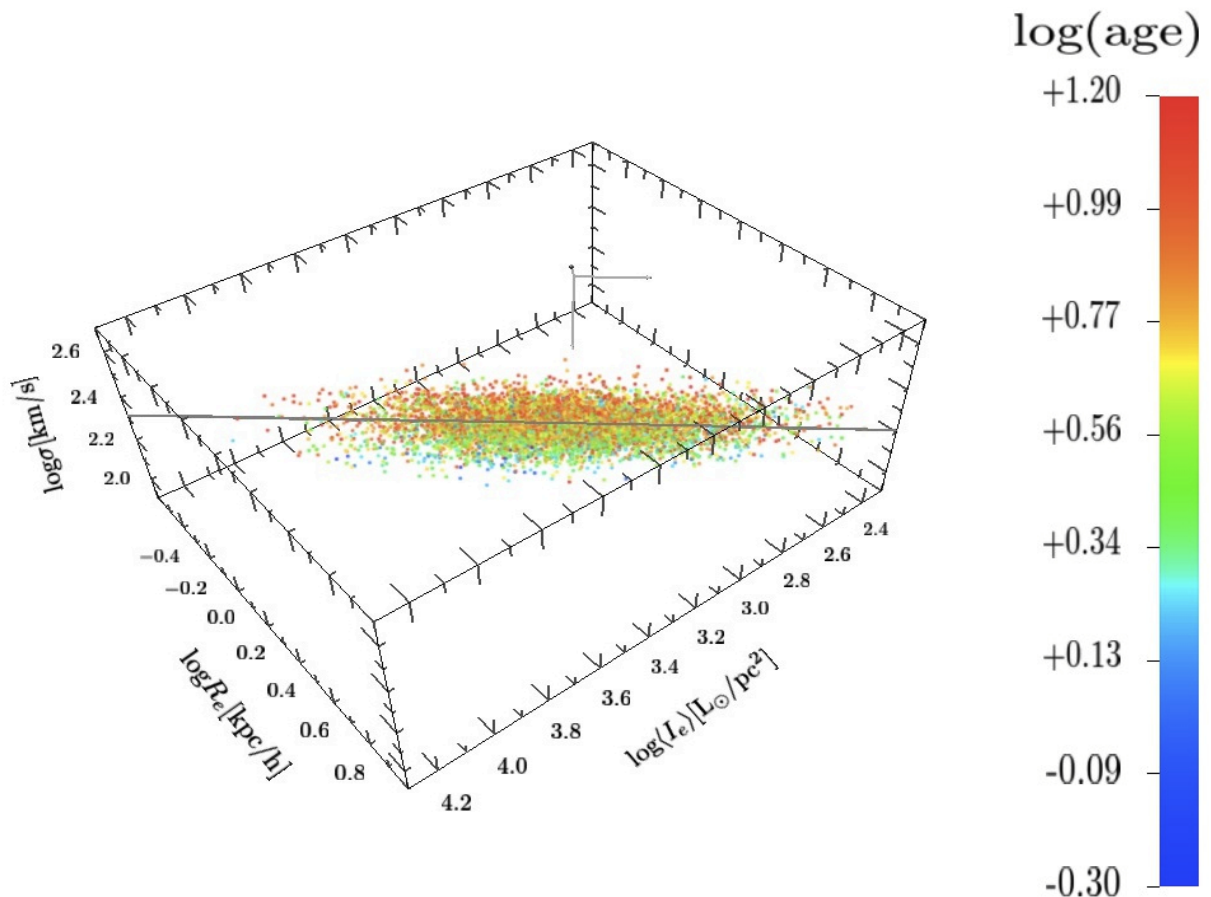$$\text{BIC} = -2\ln(\mathcal{L}) + k\ln(N) . \qquad (23)$$

Figure 12. Interactive 3D visualisation of the 6dFGS J band Fundamental Plane with individual galaxies colour-coded by $\log(\text{age})$. (Readers using Acrobat Reader v8.0 or higher can enable interactive 3D viewing of this schematic by mouse clicking on the figure; see Appendix B for more detailed usage instructions.)

The model with the lowest BIC value is preferred.

For the standard 8-parameter model of §2, the BIC value is -42075, as compared to -42287 for the 9-parameter model including an additional σ component in the $\mathbf{v_2}$ vector (§5.4) and -31833 for the 11-parameter model including age as an additional parameter (§5.5). Therefore the BIC indicates that the 11-parameter model including age is not an improvement on the standard model, as was previously concluded in §5.5. However the 9-parameter model that includes a σ-component in the $\mathbf{v_2}$ vector does have a lower BIC value than the standard 8-parameter model, and so is the objectively preferred model. We nonetheless choose to employ the standard 8-parameter 3D Gaussian model because of its simpler physical interpretation, reduced computational burden, and marginally better precision in estimating distances.

5.7 Fundamental Plane differences between passbands

Table 3 gives the best-fit FP parameters for each of the J, H and K bands. The FP slopes a and b are consistent between these passbands at about the joint 1σ and 2σ levels respectively. All three samples also have the same (small) intrinsic scatter orthogonal to the FP, $\sigma_1 = 0.05\,\text{dex}$ (12%). Figure 13 illustrates the variation with wavelength of the fitted FP slopes a and b, and also the off-

set of the FP in the r direction (the latter quantified by r_0, defined above in §5.2). The figure shows the results of fitting FPs to 1000 mock samples in each passband with input parameters given by the best-fit FP for the corresponding observed sample (as per Table 3). It also shows the mean values of the fitted parameters for the mock samples, and the 1σ and 2σ contours of their distributions. As expected, the bias-corrected mean coefficients accurately recover the input values; for reference, the coefficients of the best-fit FP for the observed J band sample are marked in each plot as a pair of dashed black lines.

The marginally significant (2σ) difference in the slopes between the J and K bands may be due to the fact that J band mass-to-light ratios are almost independent of metallicity, whereas this is not the case in the K band (Worthey 1994). In this regard it is worth noting that the J band FP is (marginally) closer to the virial plane than the K band FP.

In the central and right panels, there is a clear offset in r_0 between passbands, with r_0 increasing at longer wavelengths. We expect the differences in r_0 between passbands should be consistent with the mean colours. To quantify the mean difference in r_0 (i.e. Δr_0) as a function of mean colour and surface brightness, we assume that the FP slopes are consistent in each band (a good approximation given the similarity of the coefficients in Table 3) and
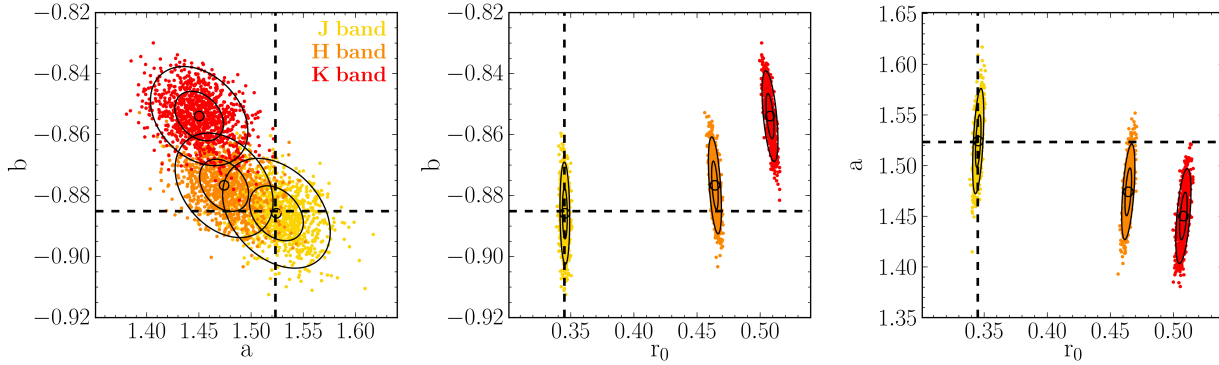
Figure 13. Uncertainties on the FP parameters for the 6dFGS J (yellow; $N_g = 8901$), H (orange; $N_g = 8568$) and K (red; $N_g = 8573$) samples. The points show the best-fit FP parameters for each of 1000 mock samples that take as input the best-fit FP parameters for the observed sample in each band. The mean values of the fitted FP parameters from the mocks, and their 1σ and 2σ contours, are also plotted. For reference, the input FP parameters used to generate the samples for the J band are indicated as dotted lines. *Left:* b versus a, showing similar FP coefficients although with a very weak trend of decreasing a and increasing b with increasing wavelength. *Centre:* b versus r_0, showing significant offsets between the FPs in the three passbands. *Right:* a versus r_0, again showing the FP offsets.

that the galaxies are homologous. These approximations lead to the following relation:

$$\Delta r_0 = b(\Delta i_0 + 0.4\langle J - H \rangle) , \qquad (24)$$

where $\langle J - H \rangle$ is the mean colour in the J and H bands (or similarly $\langle J - K \rangle$ for the J and K bands) and Δi_0 is the mean difference in i_0, the surface brightness offset of the FP at a fiducial point (here taken to be $s_0 = 2.3$ and $r_0 = 0.35$). For $b = -0.88$, the mean offset in r_0 between J and H bands (as calculated from equation 24) is -0.14 as compared to the offset of -0.12 observed directly from the fits (see the r_0 values in Table 3). Similarly, for the J and K bands, the predicted Δr_0 is -0.19, as compared to the observed offset of -0.17 from the fits.

The predicted values are very close to the offsets observed, so we conclude that the offsets in r_0 between passbands are a consequence of the mean colours, as expected. Equivalently, allowing for the mean colours the FP is consistent between the J, H and K bands.

5.8   Comparison to literature

A summary of previous FP slope determinations from the literature is given in Table 4, along with the passband, sample size and fitting method of each study. Where more than one regression method was employed, the slopes from the orthogonal regression fit are given. The coefficients of surface brightness, b, were converted to the units used in this work (i.e. as the coefficient of $i \equiv \log\langle I_e \rangle$ rather than $\langle \mu_e \rangle$, where the conversion is $b_i = -2.5b_\mu$). In those studies where an orthogonal rms scatter about the plane was quoted (based on an orthogonal regression or ML fit), we have listed this value in the $\sigma_\perp$ column and converted it to an rms scatter in the $r \equiv \log R_e$ direction using $\sigma_r = \sigma_\perp(1+a^2+b^2)^{1/2}$ (for reference, this scaling factor is 2.0 for $a = 1.5$ and $b = 0.88$). Note that the rms scatter in $r \equiv \log R_e$ in dex, δ_r, is conventionally converted to a fractional scatter in R_e in percent, σ_r, using $\sigma_r \equiv (10^{+\delta_r} - 10^{-\delta_r})/2$.

Table 4 shows the increase over time in the size of the samples being studied and also the variety of fitting techniques employed, with the more recent studies generally preferring orthogonal regression or ML fits. The fitted value of the FP coefficient of velocity dispersion, a, is typically found to be 1.2–1.4 at optical wavelengths and 1.4–1.5 in the near-infrared. *Within* individual studies in the op-

tical, a tends to be larger in redder passbands; *between* studies the differences are at least as large as this trend. By contrast, b is generally consistent with being constant across passbands within any individual study, although it varies over the range -0.74 to -0.90 when comparing different studies.

A direct comparison of the 6dFGS FP to the results of other studies is constrained by the fact that only one study uses J and H band samples (La Barbera et al. 2010a), and only two studies use K band samples (Pahre, Djorgovski & de Carvalho 1998; La Barbera et al. 2010a). Moreover, neither of these studies use a ML fitting technique, so we have chosen to compare with orthogonal regressions, where available, as the next-best fitting method. Our $s \equiv \log \sigma_0$ slope ($a = 1.52$) is consistent with the other near-infrared FP fits in being steeper than is generally found in optical passbands. Our $i \equiv \log\langle I_e \rangle$ slope ($b = -0.89$) is at the upper end of the range of previous results. Due to the large sample and homogeneous data afforded by the 6dFGS, the fractional errors on both slopes (for a less than 2% and for b less than 1%) are significantly smaller than is the case for older FP samples, and comparable to those obtained for the similarly large and homogeneous SDSS and UKIDSS samples (Hyde & Bernardi 2009; La Barbera et al. 2010a).

The most recent FP studies analysing large data sets across multiple passbands have found a steepening of the FP slope a going from shorter to longer wavelengths, while in general the slope b remains constant (Hyde & Bernardi 2009; La Barbera et al. 2010a). This trend, however, is observed across optical to near-infrared wavelengths, but (as here) not over the JHK passbands (see Table 4). This implies, as expected, that there is relatively little variation with mass or size in the dominant stellar populations (and hence the stellar M/L) across these near-infrared passbands.

The recent SPIDER FP study by La Barbera et al. (2010a) provides the closest match to 6dFGS in both sample size and passbands: we can compare the J, H and K ML Gaussian FP fits for more than 8500 6dGFS galaxies with orthogonal regression FP fits in the same bands for 4589 SPIDER galaxies. The two studies obtain almost identical values of a in the J band (1.52 and 1.53), but 6dFGS finds a to be significantly smaller in the H and K bands (1.47 and 1.46), while SPIDER finds slightly larger values in these bands (1.56 and 1.55). The differences between the two studies in the H and K band values of a are significant relative to the esti-

Table 4. Best-fitting FP slopes a and b as reported by previous studies in the literature. Also listed are the passband, sample size and fitting method used in each study. FP fits in optical and near-infrared passbands are shown respectively in the upper and lower halves of the table. Where available, the observed scatter orthogonal to the FP ($\sigma_\perp$) and the scatter about the FP in $\log R_e$ (σ_r) are given.

Survey	Band	N_g	a	b	$\sigma_\perp$	σ_r	Type of fit
Dressler et al. (1987)	B	97	1.33±0.05	−0.83±0.03	-	20%	inverse regression
Djorgovski & Davis (1987)	r_G	106	1.39±0.14	−0.90±0.09	-	20%	2-step inverse regression
Lucey et al. (1991)	V	66	1.26	−0.82	-	17%	forward regression
Guzman, Lucey & Bower (1993)	V	37	1.14	−0.79	-	17%	forward regression
Jorgensen, Franx & Kjaergaard (1996)	r	226	1.24±0.07	−0.82±0.02	-	17%	orthogonal regression
Hudson et al. (1997)	R	352	1.38±0.04	−0.82±0.03	-	21%	inverse regression
Müller et al. (1998)	R	40	1.25	−0.87	-	19%	orthogonal regression
Gibbons, Fruchter & Bothun (2001)	R	428	1.37±0.05	−0.84±0.03	-	21%	inverse regression
Colless et al. (2001)	R	255	1.22±0.09	−0.84±0.03	11%	20%	ML Gaussian
Bernardi et al. (2003)	g	5825	1.45±0.06	−0.74±0.01	13%	25%	ML Gaussian
Bernardi et al. (2003)	r	8228	1.49±0.05	−0.75±0.01	12%	23%	ML Gaussian
Hudson et al. (2004)	V\R	694	1.43±0.03	−0.84±0.02	-	21%	inverse regression
D'Onofrio et al. (2008)	V	-	1.21±0.05	−0.80±0.01	-	-	orthogonal regression
La Barbera et al. (2008)	r	1430	1.42±0.05	−0.76±0.008	15%	28%	orthogonal regression
Gargiulo et al. (2009)	R	91	1.35±0.11	−0.81±0.03	-	21%	orthogonal regression
Hyde & Bernardi (2009)	g	46410	1.40±0.05	−0.76±0.02	16%	31%	orthogonal regression
Hyde & Bernardi (2009)	r	46410	1.43±0.05	−0.79±0.02	15%	30%	orthogonal regression
La Barbera et al. (2010a)	g	4589	1.38±0.02	−0.79±0.003	-	29%	orthogonal regression
La Barbera et al. (2010a)	r	4589	1.39±0.02	−0.79±0.003	-	26%	orthogonal regression
Scodeggio, Giovanelli & Haynes (1997)	I	109	1.25±0.02	−0.79±0.03	-	20%	mean regression
Pahre, Djorgovski & de Carvalho (1998)	K	251	1.53±0.08	−0.79±0.03	-	21%	orthogonal regression
Bernardi et al. (2003)	i	8022	1.52±0.05	−0.78±0.01	11%	23%	ML Gaussian
Bernardi et al. (2003)	z	7914	1.51±0.05	−0.77±0.01	11%	22%	ML Gaussian
La Barbera et al. (2008)	K	1430	1.53±0.04	−0.77±0.008	14%	29%	orthogonal regression
Hyde & Bernardi (2009)	i	46410	1.46±0.05	−0.80±0.02	15%	29%	orthogonal regression
Hyde & Bernardi (2009)	z	46410	1.47±0.05	−0.83±0.02	15%	29%	orthogonal regression
La Barbera et al. (2010a)	J	4589	1.53±0.02	−0.80±0.003	-	26%	orthogonal regression
La Barbera et al. (2010a)	H	4589	1.56±0.02	−0.80±0.005	-	27%	orthogonal regression
La Barbera et al. (2010a)	K	4589	1.55±0.02	−0.79±0.005	-	28%	orthogonal regression
6dFGS (this paper, Table 3)	J	8901	1.52±0.03	−0.89±0.008	15%	30%	ML Gaussian
6dFGS (this paper, Table 3)	H	8568	1.47±0.02	−0.88±0.008	15%	29%	ML Gaussian
6dFGS (this paper, Table 3)	K	8573	1.46±0.02	−0.86±0.008	15%	29%	ML Gaussian

mated uncertainties (3.2σ). Within each of the 6dFGS and SPIDER studies the values of b are consistent across the three bands; however 6dFGS finds b in the range -0.89 to -0.86, while SPIDER obtains a more positive value, $b = -0.79$. This difference in b is highly significant relative to the estimated uncertainties ($>8\sigma$), but may be at least partly attributed to the fact that orthogonal regression tends to find systematically higher values of b, as shown in Figure 2.

As well as comparing the *slopes* of the FP fits, it is interesting to consider the *scatter* about the FP found in different studies. The rms scatter about the FP relation projected in the $\log R_e$ direction (σ_r in Table 4) is usually taken as an estimate of the rms uncertainty in distances and peculiar velocities when the FP is used as a distance estimator. This uncertainty is widely quoted as being 20% or even smaller, a figure reflected in Table 4 for the older FP samples. However the scatter in $\log R_e$ calculated in this way for the most recent studies (La Barbera et al. 2008; Hyde & Bernardi 2009; La Barbera et al. 2010a), and for the 6dFGS sample, is in fact almost 30%. This is somewhat surprising, given that these recent samples are large and generally contain good-quality homogeneous measurements of the FP parameters. In part the difference may be due to the fact that these larger samples may contain a more heterogeneous mix of galaxy types than the older 'hand-picked' samples (see §7 below). However a major source of this discrepancy is that

it is *not* correct to interpret the rms scatter about an orthogonal regression or ML fit, projected in $\log R_e$, as the uncertainty in distance. As discussed in detail in §8.3, if one correctly accounts for the distribution of galaxies in the FP, then the true distance error, σ_d, is significantly smaller than σ_r. For the 6dFGS sample, while the rms scatter about the FP in the $\log R_e$ direction is $\sigma_r = 29\%$, the rms scatter in the distance estimates is in fact $\sigma_d = 23\%$.

6 ENVIRONMENT AND THE FUNDAMENTAL PLANE

We investigate possible variations in the FP with *group* environment, characterised by richness, and with *local* environment, characterised by a nearest-neighbour density measure.

First, we consider potential environmental effects that correlate with the scale of the dark matter halos that galaxies inhabit, using the richness estimates from the group catalogue described in §3.4 as a proxy for halo mass. We define four subsamples according to richness N_R: galaxies in the field or very low richness groups ($N_R \leqslant 1$), galaxies in low-richness groups ($2 \leqslant N_R \leqslant 5$), galaxies in medium-richness groups ($6 \leqslant N_R \leqslant 9$), and those galaxies in high-richness groups and clusters ($N_R \geqslant 10$). There are 6495 field galaxies, 1248 in low-richness groups, 546 in medium-richness groups, and 612 in high-richness groups and clusters.

The distribution of these richness subsamples in FP space can

be viewed in the interactive 3D visualisation of Figure 14, where the galaxies in the 6dFGS J band FP sample are colour-coded by the richness of the group environment they inhabit. From examination of these distributions it is apparent that these subsamples tend to populate similar FPs. This is broadly confirmed by the best-fit FP parameters for each of these richness subsamples given in Table 3. The FP slopes a and b are similar within 1σ for all four richness subsamples and the full J band sample, and the offset of the FP, given by r_0, is similar for the three subsamples of galaxies in groups. The one significant difference is between the offset for the field galaxy subsample and the group subsamples.

These similarities and differences are clarified in Figure 15, which shows the best-fitting parameters of each richness subsample, along with the 1σ and 2σ error contours determined from 200 mock samples. The consistency of the FP slopes is shown in the left panel of this figure, while the difference in FP offsets between the field and group subsamples is shown in the centre and right panels. This offset is $\Delta r_0 \approx 0.02$ dex, which is relatively small compared to the total scatter in r of the full sample ($\sigma_r = 0.127$ dex). Nonetheless, it corresponds to a systematic size or distance offset of about 4.5%, and is statistically significant at $>3.7\sigma$. Such an offset would have an appreciable impact on estimates of the relative distances of field and group galaxies if it were not accounted for.

We repeat this analysis for the sample of 8258 galaxies for which we have local environment estimates, as described in §3.4. This sample is divided by local surface density (Σ_5) into three approximately equal-sized subsamples: 2664 galaxies in low-density environments ($\Sigma_5 \leqslant 0.07$), 2812 galaxies in medium-density environments ($0.07 < \Sigma_5 \leqslant 0.25$) and 2782 galaxies in high-density environments ($\Sigma_5 > 0.25$). We fit FPs to each of these subsamples individually, deriving the best-fit parameters given in Table 3. The coefficient of velocity dispersion, a, is similar across the three subsamples and also with respect to the global sample. There is weak variation (at the 2σ level), in the surface brightness coefficient, b, with galaxies in denser environments tending to have an FP with a shallower b slope; galaxies in the low surface density sample exhibit the largest variation in b from the global FP. However, the strongest trend with local environment is in the offset of the FP, where r_0 is systematically smaller for galaxies with higher surface density. The significance of this trend is clearly shown in the centre and right panels of Figure 16, where we plot the best-fit FP slopes, a and b, and the r_0 offset from 200 mock simulations of each local surface density subsample.

Comparing the local density FP fits illustrated in Figure 16 to those for richness shown in Figure 15, we find the same consistency in a and the same trend with environment in r_0. The trend in b as a function of local surface density is not seen for global environment, although this may possibly be because our higher richness subsamples have too few galaxies to recover such a weak trend.

Suggestions of environmental dependence in the FP (or the $D_n-\sigma$ relation) first emerged in studies where a weak offset between galaxies in clusters (such as Coma and Virgo) and the field was detected (Lucey, Bower & Ellis 1991; de Carvalho & Djorgovski 1992). However it was later suggested that these differences could be attributed to errors in measurement, as no such offset in the FP was subsequently found between field and cluster galaxies in other similar studies (Burstein, Faber & Dressler 1990; Lucey et al. 1991; Jorgensen, Franx & Kjaergaard 1996). As samples of early-type galaxies increased, and the range covered in environment and mass was extended, trends with environment were found for *local* density indicators such as cluster-centric distance (Bernardi et al. 2003) and local galaxy density (D'Onofrio et al. 2008). The lat-

ter study also found a strong trend in the FP slopes a and b with *local* galaxy density, but no trend with *global* environment parameters such as richness, R_{200} and velocity dispersion. More recently, La Barbera et al. (2010c) explored the role of environment in the FP and found a strong trend with local galaxy density (and a weaker trend with normalised cluster-centric distance), independent of passband. Evidence of this trend is indicated by a lower offset of the FP for galaxies in high-density regions compared to low-density regions, consistent with previous results (Bernardi et al. 2003; D'Onofrio et al. 2008). The slope a was found to decrease in high-density regions (in all passbands), while b tended to weakly increase with local galaxy density (a trend that disappears in the near-infrared). Similar trends in the FP parameters were found for galaxies in groups and the field.

The results obtained for the 6dFGS sample are consistent with other recent studies, in that the variation of the FP is more pronounced for parameters that reflect *local* density or environment than for those that are proxies for *global* environment. Even though we compare the offset between FPs using r_0 rather than c (as La Barbera et al. 2010c do), the trend we find with surface density (i.e. lower r_0 for galaxies in higher-density environments), is at least qualitatively consistent with that of the SPIDER study. However, to anticipate the discussion in §8.5, these variations in the FP with environment are smaller than the variation found with age; if the age of the stellar population were the main driver of FP variations, then the environmental variations might be primarily the result of correlations between environment and stellar population.

7 MORPHOLOGY AND THE FUNDAMENTAL PLANE

We examine the morphological variation of the Fundamental Plane using a visual classification of each galaxy's morphology from multiple people, as described in §3.5. The J band FP sample was divided into two morphological subsamples: 6956 elliptical and lenticular galaxies (those classified as E, E/S0 or S0) and 1945 early-type spiral bulges (those classified as S0/Sp or Sp and having bulges filling the 6dF fibre aperture). Note that the initial NIR selection criteria mean there are relatively few of the latter class, and that these may have some degree of bias towards larger $\log R_e$. We do not separate the E and S0 galaxies into separate subsamples since there is significant overlap in our morphological classifications for these two classes. We note that the FP is, in general, found to be consistent between samples of E and S0 galaxies (Jorgensen, Franx & Kjaergaard 1996; Colless et al. 2001), and that, in fitting the E and S0 galaxies as one morphological subsample, we find the same scatter about the FP as the for full sample.

Figure 17 is an interactive 3D visualisation of the J band FP sample colour-coded by morphology, with the ellipticals and lenticulars in red and the early-type spiral bulges in blue. This figure shows that the two morphological subsamples populate slightly different locations *within* the FP, with the early-type spiral bulges more common at larger $\log R_e$.

The best-fit FP parameters for these two subsamples are given in Table 3, and their relative values and errors are illustrated using mock samples in Figure 18. The figure shows that the FP slopes, a and b, are consistent for the different morphological classes but that the offset in $\log R_e$, while small ($\Delta r_0 = 0.045$ dex) relative to the overall scatter in $\log R_e$, is highly significant (7σ) and corresponds to a systematic error of 10% in sizes and distances. An offset of this amplitude would have a substantial impact on esti-
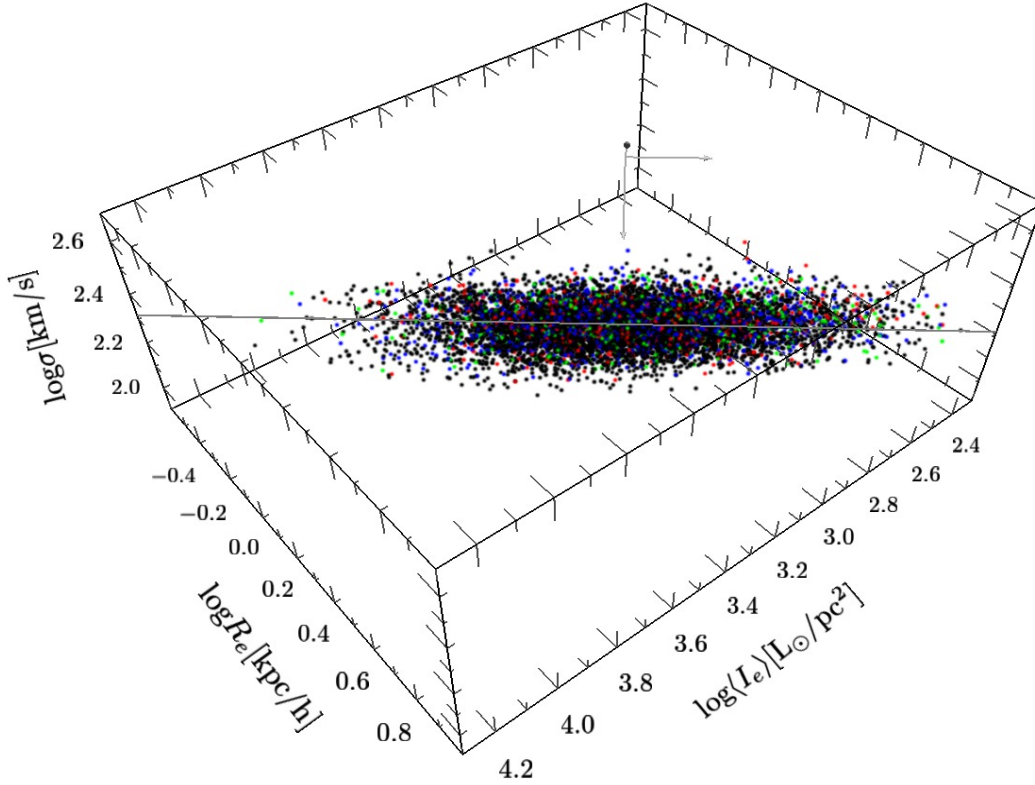
Figure 14. Interactive 3D visualisation of the 6dFGS J band Fundamental Plane with individual galaxies colour-coded by the richness of the group environment they inhabit: 6495 field galaxies in black; 1248 galaxies in low-richness groups in blue; 546 galaxies in medium-richness groups in green; and 612 galaxies in high-richness groups in red (these richness classes are defined in the text). The best-fitting plane (in grey) for the entire sample (with $a = 1.523$, $b = -0.885$ and $c = -0.330$) is shown for reference. (Readers using Acrobat Reader v8.0 or higher can enable interactive 3D viewing of this schematic by mouse clicking on the figure; see Appendix B for more detailed usage instructions.)

Figure 15. As for Figure 13, but comparing the FP fits to four richness samples spanning field (grey; $N_g = 6495$), low richness (blue; $N_g = 1248$), medium richness (green; $N_g = 546$) and high richness (red; $N_g = 612$) galaxy samples. The points in each panel are the fits to 200 mocks of each of these four subsamples; the large black circles show the means and the ellipses the 1σ and 2σ contours of the distribution of fitted parameters. The dashed lines show, for reference, the best-fit parameters for the full J band sample.

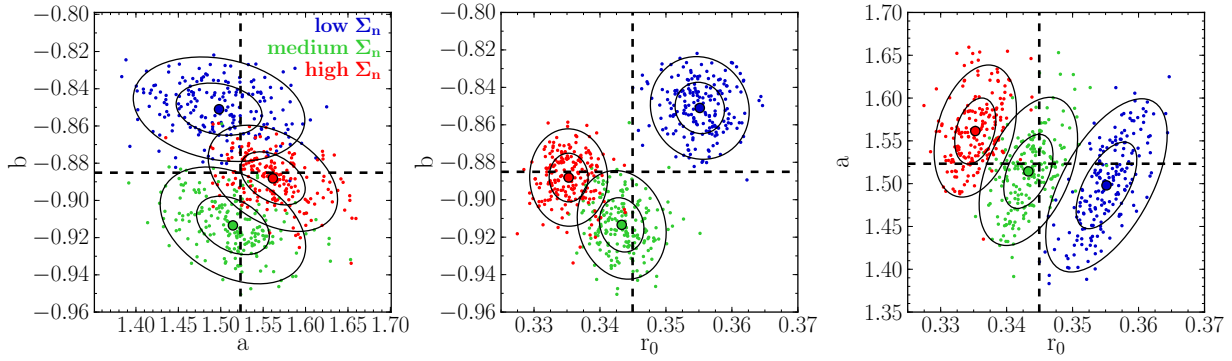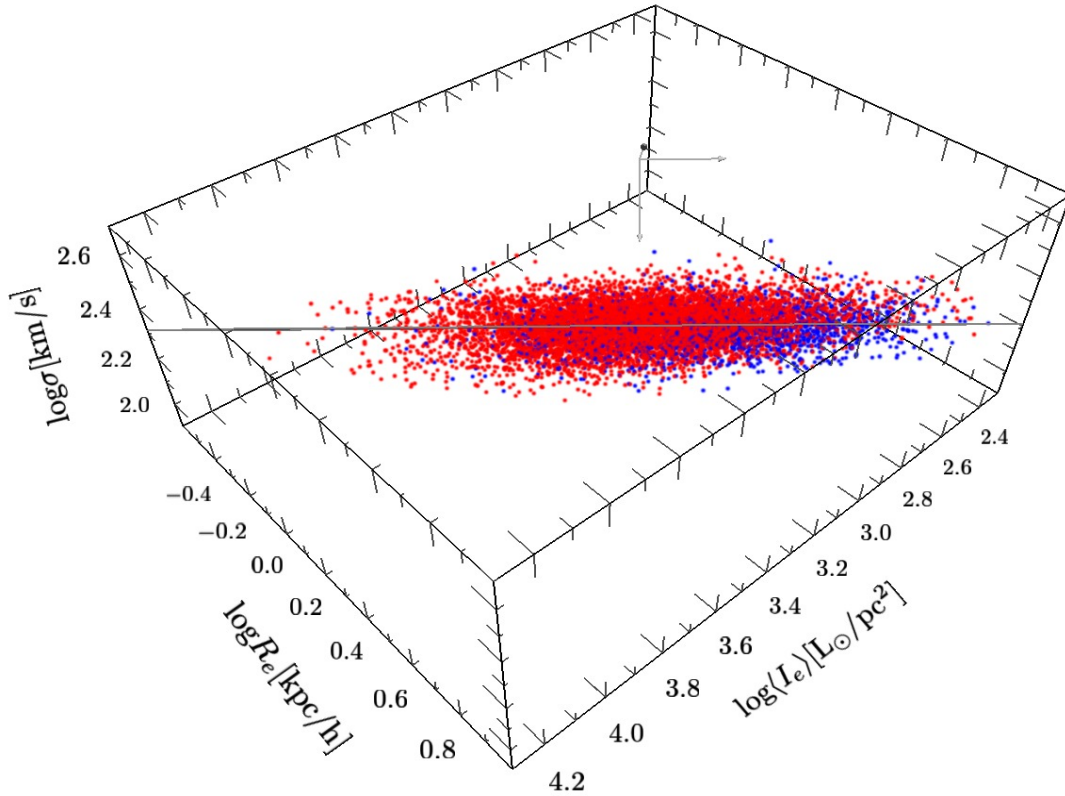**Figure 16.** As for Figure 13, but comparing the FP fits to three local surface density, Σ_5, samples spanning low Σ_5 (blue; $N_g = 2664$), medium Σ_5 (green; $N_g = 2812$) and high Σ_5 (red; $N_g = 2782$) galaxy samples. The points in each panel are the fits to 200 mocks of each of these three subsamples; the large black circles show the means and the ellipses the 1σ and 2σ contours of the distribution of fitted parameters. The dashed lines show, for reference, the best-fit parameters for the full J band sample.

Figure 17. Interactive 3D visualisation of the 6dFGS J band Fundamental Plane in $(\mathbf{r}, \mathbf{s}, \mathbf{i})$-space. The best-fitting plane (in grey) for the J band (with $a = 1.523$, $b = -0.885$ and $c = -0.330$) is plotted for reference. The galaxies are colour-coded according to morphology: 6956 early types in red and 1945 late types in blue. (Readers using Acrobat Reader v8.0 or higher can enable interactive 3D viewing of this schematic by mouse clicking on the figure; see Appendix B for more detailed usage instructions.)

mates of the relative distances of E/S0 galaxies and Sp bulges if it were not accounted for.

In addition to the difference in FP offset, there is a large shift in the centroid of the distribution *within* the FP, with the early-type spiral bulges having $\bar{r} = 0.304$ while the ellipticals and lenticulars have $\bar{r} = 0.155$; i.e. the spiral bulges are typically 35% larger. We

speculated that this may be due to the selection criteria imposed, namely that the spiral bulges had to fill the 6dF fibre apertures. We therefore re-sampled the elliptical/lenticular sample to have the same apparent size distribution as the spiral bulges, and re-fit the FP to this subsample; this did not induce an offset in r_0 as observed in the spiral bulges. We conclude that this offset is not primarily a
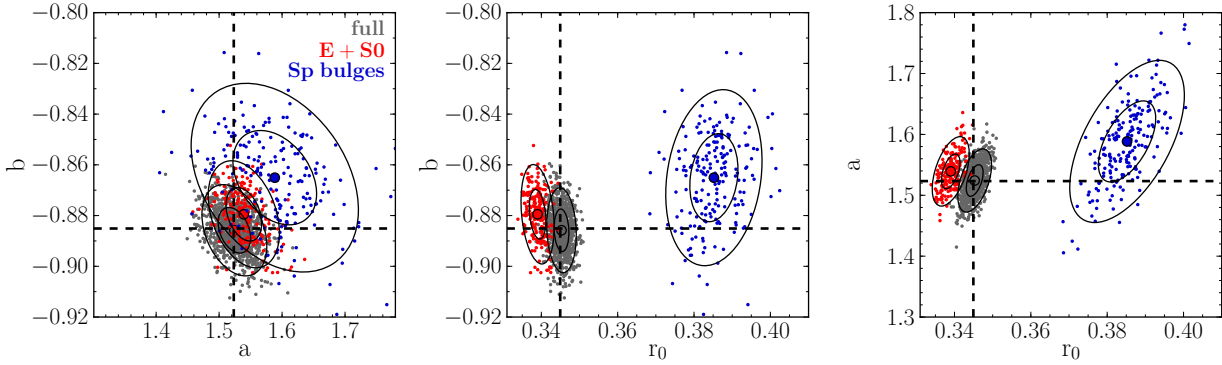
Figure 18. As for Figure 13 but comparing the FP fits to the two morphological subsamples: 6956 elliptical and lenticular galaxies (E/S0) in red and 1945 early-type spiral bulges (Sp bulges) in blue; the full J band sample of 8901 galaxies is shown in grey. The points in each panel are the fits to 200 mocks of the two morphological subsamples and to 1000 mocks of the full sample; the large black circles show the means of the fitted parameters and the ellipses show the 1σ and 2σ contours of the distribution. The dashed lines show, for reference, the best-fit parameters for the full observed J band sample.

selection effect, but rather a real difference between the FPs of the ellipticals/lenticulars and the early spiral bulges.

8 DISCUSSION

8.1 The Fundamental Plane as a 3D Gaussian

Although throughout this paper we emphasise the value of fitting a 3D Gaussian model to the FP, this is *not* saying that the intrinsic FP is necessarily Gaussian. That may be the case in some axes, but in others (e.g. in luminosity or velocity dispersion) the intrinsic distribution very likely takes some other form (such as a Schechter function)—a form that is only approximated by a Gaussian over the range of values in our sample (i.e. the bright/large/massive end of the distribution).

We have chosen to use a Gaussian model because it is computationally easy and because empirically it fits the data in our sample (as evidenced by Figure 8). In practice the observed FP is consistent with (well modelled by) a Gaussian partly due to either (or both) the sample selection criteria and the observational errors. The errors are approximately Gaussian and are relatively large in the raw quantities r, s and i (although not in some combined quantities like $r - bi$). Convolving these errors with the intrinsic FP results in a more Gaussian distribution.

This effect is compounded by the selection criteria. For example, the velocity dispersion cutoff truncates the probable Schechter function of the intrinsic distribution in such a way that the truncated distribution can be fit by a truncated Gaussian (the exponential part of a Schechter function is similar to a Gaussian that is truncated near its peak). This truncated distribution is then blurred and made more Gaussian by the observational errors.

In sum, although a Gaussian intrinsic distribution is statistically a sufficiently good model for the data in the 6dFGS sample (as well as being computationally convenient), the substantial effects due to the sample selection criteria and observational errors mean that we cannot conclude that the underlying physical distribution is Gaussian. While the ML method successfully fits a Gaussian to the intrinsic FP distribution, a more realistic distribution might fit as well or better.

8.2 Fundamental Plane scatter

In general, the total scatter in r that we recover for the 6dFGS FP ($\sigma_r \approx 29\%$) is comparable to that found in other recent studies (Gargiulo et al. 2009; Hyde & Bernardi 2009; La Barbera et al. 2010a), but larger than the value typically quoted as the FP distance error ($\sigma_r \sim 20\%$) found in earlier studies (see Table 4). However, it is important to note that the larger value of σ_r found in recent studies (and here) is the rms scatter, projected along the r-direction, about the best-fitting orthogonal or maximum-likelihood FP. In §8.3, we show that this over-estimates the actual FP distance errors.

Here we examine the individual components contributing to the overall scatter about the FP. This scatter results from a combination of intrinsic scatter in the FP relation (the physical origins of which are subject to investigation), observational errors and contamination from outliers (such as non-early-type galaxies or merging objects). To understand how each of these contribute to the total rms scatter in r, we split σ_r into the quadrature sum of these components:

$$\sigma_r^2 = (a\epsilon_s)^2 + \epsilon_X^2 + \sigma_{r,int}^2 . \tag{25}$$

The first term represents the effect of the rms observational scatter in velocity dispersion, ϵ_s, on the overall scatter in r. Because ϵ_s is scaled by a, the FP coefficient of s, this term is larger for samples with larger FP slopes. Since a tends to increase with wavelength ($a \approx 1.2$–1.4 in optical passbands and $a \approx 1.4$–1.5 in near-infrared passbands), this term is generally larger for near-infrared selected samples (such as 6dFGS) than for optically selected samples (such as SDSS). The rms velocity dispersion error of the 6dFGS sample is $\epsilon_s = 0.054$ dex (i.e. 12%, comparable to other large survey samples; see Campbell 2009). So, given our J band slope of $a = 1.52$, this term amounts to a contribution to the overall scatter of about 18%. To more directly determine the effect of the errors in s on the FP fits, we have fitted subsamples restricted to smaller ϵ_s values (see Table 5). We find no change in the FP slopes (at the 1σ level), a small but significant change in the offset, and a modest reduction (at most 5%) in the overall scatter in $\log R_e$, consistent with that expected from the smaller value of ϵ_s and the above formula for the total scatter.

The second term in equation 25 is the rms observational scatter in the combined photometric quantity $X_{\rm FP} \equiv r - bi$, which accounts for the high degree of correlation between the measurement

Table 5. Best-fit FP dependence on velocity dispersion error.

ϵ_s	N_g	a	b	r_0	σ_r
no limit	8901	1.523±0.026	-0.885±0.008	0.345±0.002	0.127
⩽0.07	7913	1.523±0.026	-0.896±0.009	0.346±0.002	0.124
⩽0.06	6694	1.529±0.029	-0.903±0.010	0.349±0.002	0.122
⩽0.05	4692	1.528±0.032	-0.909±0.011	0.356±0.003	0.118
⩽0.03	1855	1.558±0.053	-0.894±0.018	0.376±0.005	0.108

errors in r and i (see §3.3). This correlation conspires to make the value of this term negligible in comparison to the other terms; for all the 6dFGS passbands, $\epsilon_X \leqslant 4\%$.

The final term represents the intrinsic scatter of the FP relation in the r direction. For a pure 3D Gaussian distribution the intrinsic scatter in r would be given by $\sigma_r = \sigma_1(1+a^2+b^2)^{1/2}$, which, for our typical values of $a = 1.5$ and $b = -0.88$, yields $\sigma_r \approx 2.0\,\sigma_1$. However, because our observed distribution is heavily censored by our selection criteria, the actual distribution of galaxies in FP space is a truncated 3D Gaussian, and so we cannot apply this formula. Instead we must calculate σ_r either from equation 25, taking the difference between the total scatter and the rms measurement errors, or as the rms scatter in $r - as - bi$ for mock samples drawn from the same intrinsic 3D Gaussian and the same selection criteria, but with no measurement errors. Both these approaches yield the same estimate for the intrinsic scatter in r for our J band sample: $\sigma_{r,int} \approx 23\%$. The intrinsic scatter is therefore the single largest contributor to the overall scatter about the 6dFGS FP.

Thus we have our total scatter in r of 29% being the quadrature sum of 18% scatter from the measurement errors in velocity dispersion, 4% scatter from the measurement errors in the photometric quantities, and 23% scatter from the intrinsic dispersion of the FP distribution.

8.3 Distance errors

We have found that the scatter about the 6dFGS FP in r is 29%. However, this does *not* mean that, when we use this FP fit to measure distances, we will only measure them to this precision. To understand why this is the case, we must consider the procedure used to measure distances and peculiar velocities from the FP.

In the most naive approach, one would convert the observed angular radius of a galaxy to a physical radius assuming that the distance to the galaxy is given by its redshift distance. The peculiar velocity of the galaxy would then be approximated by the offset of this galaxy from the FP in r. Since the peculiar velocity is measured from the offset along the r-direction, the average scatter from the FP in r then represents the total error in galaxy distances and peculiar velocities (from the combination of measurement errors and intrinsic scatter).

However there is a more general (and precise) way to estimate the peculiar velocity. The peculiar velocity of a galaxy n is given by its offset along the r-direction from a particular value, r_n^*. This r_n^* is the most likely radius for galaxy n, given a particular set of observed values of the velocity dispersion and surface brightness, s_n and i_n. In the preceding paragraph, we assumed that r_n^* is a point on the FP, given by $r_n^* = as_n + bi_n + c$. This assumption is valid if the FP is best modelled as an infinite plane with uniform scatter. However, the assumption is *not* valid if the distribution of galaxies in FP space is best modelled by a 3D Gaussian and the minor axis of this Gaussian is not aligned with the r-axis.

In equation 4, we show the expression for the probability density distribution of a single galaxy n. In equation 8, we give the sum of the log of such probability densities for all galaxies in our sample. For a single galaxy n, however, the likelihood is

$$\ln(P(\mathbf{x_n})) = -\left[\frac{3}{2}\ln(2\pi) + \ln(f_n) + \frac{1}{2}\ln(|\mathbf{\Sigma} + \mathbf{E_n}|)\right.$$
$$\left. + \frac{1}{2}\mathbf{x_n^T}(\mathbf{\Sigma} + \mathbf{E_n})^{-1}\mathbf{x_n}\right]. \tag{26}$$

For a particular galaxy with known observational errors, each of these terms is fixed except the final χ^2 term, which is a quadratic function of the physical parameters r, s and i.

Since we directly observe s and i, we can fix them at the observed values s_n and i_n. We can then use this equation to give us the probability density distribution of r for fixed $s = s_n$ and $i = i_n$ (i.e. $P(r|s,i)$). This is a quadratic function of the form

$$\ln(P(r|s,i)) = k_0 + k_1(r - \bar{r}) + k_2(r - \bar{r})^2 \tag{27}$$

where k_0, k_1 and k_2 are functions of s_n, i_n, the observational errors for the galaxy, and the FP fit parameters (a, b, $\bar{r}$, $\bar{s}$, $\bar{i}$, σ_1, σ_2, and σ_3). They can thus be obtained by expanding the matrix multiplication terms in the preceding equations. The effective expectation value for galaxy distances and peculiar velocities occurs at the maximum likelihood—i.e. the maximum of this quadratic function,

$$r^* - \bar{r} = -k_1/(2k_2). \tag{28}$$

This value varies from galaxy to galaxy, depending both on the galaxy's position in FP space and its observational errors. If we evaluate this in the case of no errors, and insert the values of the FP fit parameters given in Table 3 for the J band sample, we find that the effective expectation value for distances is given by the plane $r^* = 1.18s - 0.80i + 0.152$; this relation differs quite markedly from the underlying Fundamental Plane. However, since we do in fact have observational errors, and they vary from galaxy to galaxy, the peculiar velocity expectation values for individual galaxies will *not* be confined to a plane.

We have evaluated this J band zeropoint (i.e. the maximum likelihood distance) for every galaxy in our sample, and find that the scatter about the zeropoint is 23%. This, then, is the distance error in the J band assuming no Malmquist bias corrections; we therefore anticipate that 23% does not necessarily represent our final distance error, which will be explored in a future paper.

This 23% scatter in distance is significantly smaller than the 29% that is naively obtained by calculating the scatter in r about the best-fit FP. The difference is purely a consequence of the fact that, in our empirically well-justified 3D Gaussian model for the distribution in FP space, galaxies are not symmetrically distributed about the FP in the r direction. Thus for fixed s and i the probability density of galaxies in r is not maximised on the FP, the expectation value for the observed distance is not the redshift distance, the expectation value of the peculiar velocity is not zero, and the scatter in distance and peculiar velocity relative to this expectation value is less than the scatter relative to the FP.

8.4 The Fundamental Plane in κ-space

Bender, Burstein & Faber (1992) proposed studying the FP using κ-space, a coordinate system related to key physical parameters such as galaxy mass (M) and luminosity (L). Bender et al. took as their observed parameters $\log \sigma_0^2$, $\log I_e$ and $\log R_e$ (with σ_0 in units of km s^{-1}, R_e in units of kpc and I_e in units of L$_\odot$ pc^{-2})
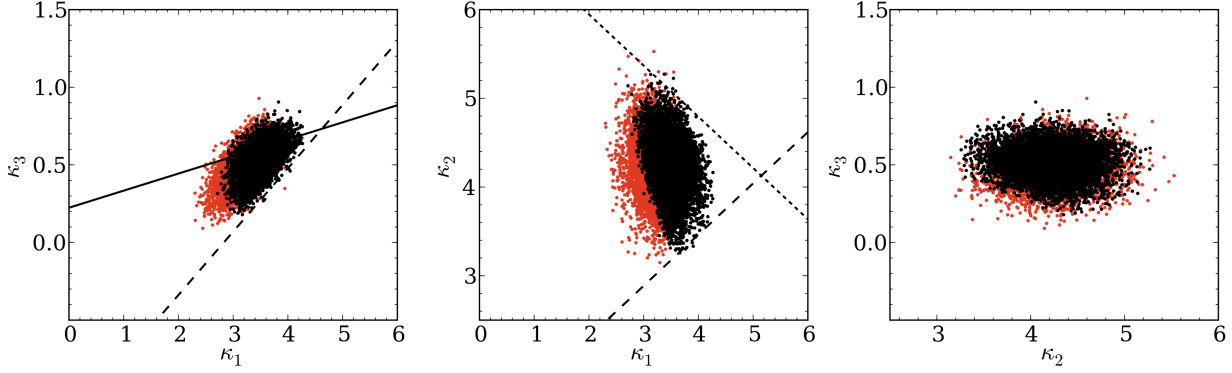
Figure 19. The κ-space distribution of the 6dFGS J band FP sample (black) and the galaxies excluded by our selection criteria from a corresponding mock sample (red). *Left:* the κ_3–κ_1 projection of the FP showing the best-fit relation ($\kappa_3 \propto 0.110\kappa_1$, solid line) and the lower limit on M/L as a function of mass ($2\sqrt{3}\kappa_3 - \sqrt{2}\kappa_1 > -4.0$; long-dashed line). *Centre:* the κ_2–κ_1 projection showing the upper limit defining the 'zone of exclusion' for dissipation ($\kappa_1 + \sqrt{3}\kappa_2 < 12.3$; short-dashed line), similar to that proposed by Bender, Burstein & Faber (1992); also the apparent lower limit on luminosity density ($\sqrt{3}\kappa_2 - \kappa_1 > 2.0$; long-dashed line). *Right:* the κ_3–κ_2 projection.

and defined κ-space in terms of the orthogonal set of basis vectors given by

$$\kappa_1 \equiv (\log \sigma_0^2 + \log R_e)/\sqrt{2} = (2s + r)/\sqrt{2},$$
$$\kappa_2 \equiv (\log \sigma_0^2 + 2\log I_e - \log R_e)/\sqrt{6} = (2s + 2i - r)/\sqrt{6},$$
$$\kappa_3 \equiv (\log \sigma_0^2 - \log I_e - \log R_e)/\sqrt{3} = (2s - i - r)/\sqrt{3}.$$
$$(29)$$

In this coordinate system, κ_1 is proportional to $\log M$, κ_2 is proportional to $\log(I_e^3 M/L)$ and κ_3 is proportional to $\log(M/L)$.

FP samples in κ-space (Bernardi et al. 2003; Burstein et al. 1997; Kourkchi et al. 2012) are often plotted in the κ_3–κ_1 projection (to show an almost edge-on view of the FP) and the κ_2–κ_1 projection (to show an almost face-on view of the FP). Figure 19 shows the κ-space distribution for the J band 6dFGS FP sample (black points) in all three 2D projections of κ-space. The galaxies rejected from a mock set of galaxies by the 6dFGS sample selection criteria are also shown (in red) to illustrate the effects of censoring on the observed κ-space distribution.

We can compute the principal axes of the FP distribution in (r, s, i)-space, (v_1, v_2, v_3), in terms of $(\kappa_1, \kappa_2, \kappa_3)$ using the inverse of the transform defined by equation 29 to map from κ-space to (r, s, i)-space followed by the transform defined by equations 5 & 6 to then map to (v_1, v_2, v_3). Inserting the values of a and b for the best-fit J band FP given in Table 3, we obtain

$$v_1 = +0.083\kappa_1 + 0.002\kappa_2 - 0.754\kappa_3 \,,$$
$$v_2 = -0.469\kappa_1 + 0.882\kappa_2 - 0.050\kappa_3 \,,$$
$$v_3 = -0.631\kappa_1 - 0.312\kappa_2 + 0.422\kappa_3 \,. \qquad (30)$$

As expected, v_1 (the direction normal to the FP) is very close to κ_3, which is proportional to $\log M/L$. However, because the transformation from (r, s, i)-space to κ-space is non-orthogonal, there is significant mixing in κ-space between v_1 and v_3, with $v_1 \cdot v_3 = -0.6$.

In κ-space the best-fit J band FP derived in (r, s, i)-space is given by

$$\kappa_3 = 0.110\kappa_1 + 0.002\kappa_2 + 0.216 \,. \qquad (31)$$

This is significantly shallower than the relation found by Bender, Burstein & Faber (1992), which was $\kappa_3 \propto 0.15\kappa_1$ (although the difference is in part due to the fact that Bender et al. were working in the B band and the 6dFGS result is for the J band). Because the

coefficient of κ_2 is so small, equation 31 is essentially a relation between $\kappa_3 \propto \log M/L$ and $\kappa_1 \propto \log M$. Neglecting the κ_2 term and using the definitions of κ_1 and κ_3 given in equation 29 yields

$$\frac{\log M/L}{\sqrt{3}} = 0.110\frac{\log M}{\sqrt{2}} + constant \,, \qquad (32)$$

which corresponds to $M/L \propto M^{0.135}$.

It is illuminating to derive this same relationship starting from the *assumption* that mass-to-light ratio has a simple power-law dependency on mass. Letting $m = \log M$ and $l = \log L$, and assuming that (ignoring constants) $m = 2s + r$ and $l = 2r + i$, if the mass-to-light ratio is a power of mass, $m - l = \alpha m$, then we can write the FP as

$$r = 2\left(\frac{1 - \alpha}{1 + \alpha}\right)s - \left(\frac{1}{1 + \alpha}\right)i + constant \,. \qquad (33)$$

By equating FP coefficients with equation 2 we get two relations for α, namely $\alpha = (2 - a)/(2 + a)$ and $\alpha = -(1 + b)/b$. For an arbitrary FP relation there is no requirement that these two relations give consistent values for α. However, as it happens, for the particular values $a \approx 1.52$ and $b \approx -0.88$ that are very close to the best-fit J band FP for the 6dFGS sample, these relations give consistent values of $\alpha \approx 0.136$. Hence our best-fit FP is consistent with (but does not require) a simple scenario in which mass-to-light ratio is a power of mass, namely $M/L \propto M^{0.136}$ (or, equivalently, $M/L \propto L^{0.157}$).

This relation (strictly, the relation given by equation 31 with κ_2 fixed at its mean value of 4.2) is shown as the solid line in Figure 19. Because the transformation from $(\kappa_1, \kappa_2, \kappa_3)$ is, by definition, orthogonal to $(r, 2s, i)$ but *not* orthogonal to (r, s, i), the transformation from (r, s, i)-space to κ-space does not preserve the shape of the 3D Gaussian. Consequently this linear relation is not a particularly compelling description of the κ-space distribution, even though the transformed 3D Gaussian fit is still a good match to the data (as shown by the mock galaxy sample).

The 6dFGS galaxies respect the zone of exclusion in the κ_1–κ_2 plane suggested by Bender, Burstein & Faber (1992), corresponding to an upper limit on the amount of dissipation that a hot stellar system of a given mass undergoes. This limit is indicated by the short-dashed line in the centre panel of Figure 19, given by $\kappa_1 + \sqrt{3}\kappa_2 < 12.3$. The long-dashed line in the same panel provides another limit, $\sqrt{3}\kappa_2 - \kappa_1 > 2.0$, corresponding to a lower

bound on the luminosity density, L/R^3 of an early-type galaxy of a given mass. However this requires further investigation, as more compact galaxies may be catalogued in the 2MASS database as stars and consequently would be excluded from our study. The sharpest and most striking limit is that indicated by the long-dashed line in the left panel of Figure 19, $2\sqrt{3}\kappa_3 - \sqrt{2}\kappa_1 > -4.0$. This implies that for these early-type galaxies there is a minimum mass-to-light ratio that increases with increasing mass as $(M/L)_{min} \propto M^{1/2}$. Since these galaxies all have similar stellar populations, this suggests that more massive galaxies have a maximum stellar-to-total mass ratio that decreases as $M^{-1/2}$.

8.5 Fundamental Plane residual trends

In §6 and §7 we examined the dependence of the 6dFGS FP on environment and morphology by comparing the FP fits for appropriate subsamples of galaxies. Here we take an alternative approach by looking at the trends of the orthogonal residuals from the FP (defined as $[r - (as + bi + c)]/\sqrt{1 + a^2 + b^2})$ with various galaxy properties. As well as morphology, group richness ($\log N_R$) and local density ($\log \Sigma_5$), we also consider three stellar population parameters discussed in Springob et al. (2012): $\log$ age, metallicity ([Z/H]) and alpha-enhancement ([α/Fe]). For this particular purpose we convert our morphological classification scheme to a discrete scale where 0 = elliptical, 2 = lenticular, 4 = spiral and 1, 3 and 5 are the respective transition classes.

Figure 20 shows the mean residuals orthogonal to the best-fit global J band FP (with $a = 1.52$ and $b = -0.89$) as a function of these properties. The mean orthogonal residuals are computed in bins of $\log \Sigma_5$ (for 8258 galaxies), morphological type and $\log N_R$ (for 8901 galaxies), and $\log$ age, [Z/H] and [α/Fe] (for 6679 galaxies). A weighted least-squares regression is performed to quantify the significance of a linear trend in the binned data. The slope and offset of the linear fit for each galaxy property (and their errors) are given at the top of each panel, along with the reduced χ^2 of the fit.

The strongest trend of the FP residuals is clearly with the age of the stellar population, and amounts to ~ 0.08 dex over the full range in age; the next strongest trend is with [α/Fe], amounting to ~ 0.05 dex over the observed range. Both these trends are highly statistically significant, although a line is not a good fit to the relation in the case of [α/Fe]. The residuals from the FP show relatively weaker (although still statistically significant) trends with morphological type, local density, group richness and metallicity. These results are consistent with our fits to subsamples defined on the basis of these properties, and confirm the equivalent analysis by Springob et al. (2012). We refer the interested reader to that paper for a more extensive investigation of the variations of stellar populations in FP space, including a detailed comparison to the similar study by Graves, Faber & Schiavon (2009), Graves & Faber (2010) and Graves, Faber & Schiavon (2010).

If galaxy ages could be precisely determined, then these results imply that it would be possible to reduce the intrinsic scatter about the FP by a few percent. However the substantial uncertainties in estimating the ages of stellar populations mean that even this modest gain cannot be realised with current observational data and existing stellar population models.

9 CONCLUSION

The 6dFGS Fundamental Plane sample comprises $\sim 10^4$ early-type galaxies from the 6dF Galaxy Survey. We provide the first compre-

hensive visualisation for the entire Fundamental Plane (FP) parameter space (without projection) by displaying this large and homogeneous dataset in fully-interactive 3D plots.

We demonstrate that significant biasing can occur when deriving a best-fit FP using least-squares regression (the predominant fitting method used in previous studies). Standard regression techniques implicitly assume models that fail to accurately represent the underlying distribution of galaxies in FP space, and moreover do not fully account for observational errors and selection effects that tend to bias the best-fit plane. We show that a 3D Gaussian provides an excellent empirical match to the distribution of galaxies in FP space for the 6dFGS sample, and we use a maximum likelihood fitting technique to properly account for all the observational errors and selection effects in our well-characterised sample.

With this approach we obtain a best-fit FP in the 2MASS J band of $R_e \propto \sigma_0^{1.52 \pm 0.03} I_e^{-0.89 \pm 0.01}$. Fits in the H and K bands are consistent with this at the 1σ level once allowance is made for differences in mean colour, implying that M/L variations along the FP are consistent among these near-infrared passbands.

We deconstruct the scatter in r about the FP, σ_r, into contributions from observational errors and intrinsic scatter, and find that the overall scatter of 29% is the quadrature combination of an 18% observational contribution and a 23% intrinsic contribution. The observational contribution is strongly dominated by the velocity dispersion errors, and compounded by the fact that the FP slope is steeper in near-infrared passbands than in optical passbands—the FP coefficient of σ_0 is $a \approx 1.5$ for J, H and K and $a \approx 1.2$–1.4 for B, V and R, so the same error on σ_0 contributes 15–50% more scatter to σ_r for the near-infrared FP than the optical FP.

The overall scatter in R_e about the 6dFGS FP is larger than the widely-quoted value of 20%, but in fact is consistent with virtually all recent studies of large samples of galaxies (see Table 4). Moreover, the actual scatter in distance estimates is *not* the same as the scatter in R_e about the best-fit maximum-likelihood FP. We show that the true scatter in distance (and peculiar velocity) must be calculated relative to the expectation value of the distance (and peculiar velocity), which does *not* lie in the FP. This is because our empirically-validated 3D Gaussian model of galaxies in FP space has an *asymmetric* distribution about the FP in the r-direction. Consequently, the expectation value of the distance (and peculiar velocity) lies in a plane with a shallower slope than the actual FP. When the scatter is properly computed relative to this expectation value, we find that the rms scatter in distance (or peculiar velocity) is in fact 23% (neglecting any corrections for Malmquist bias).

We investigate possible changes in the FP with environment, looking for variations with both global environment (quantified by group or cluster richness) and local environment (quantified by the surface density to the fifth-nearest neighbour). We find little variation of the 6dFGS FP slopes (i.e. the coefficients of velocity dispersion and surface brightness) with either of these measures of environment. However there is a statistically and physically significant offset of the FP with environment in the sense that, at fixed velocity dispersion and surface brightness, galaxies in the field and low-density regions are on average about 5% larger than those in groups and higher-density regions.

Morphological classification of our FP sample allows us to separate the galaxies into two broad types: elliptical (E) and lenticular (S0) galaxies are combined into one subsample and early-type spiral (Sp) galaxies define the other type. For the latter, the construction of our sample means that we are effectively determining the FP parameters for the bulges of these galaxies. We find that this sample of early-type Sp bulges has FP slopes and scatter consis-
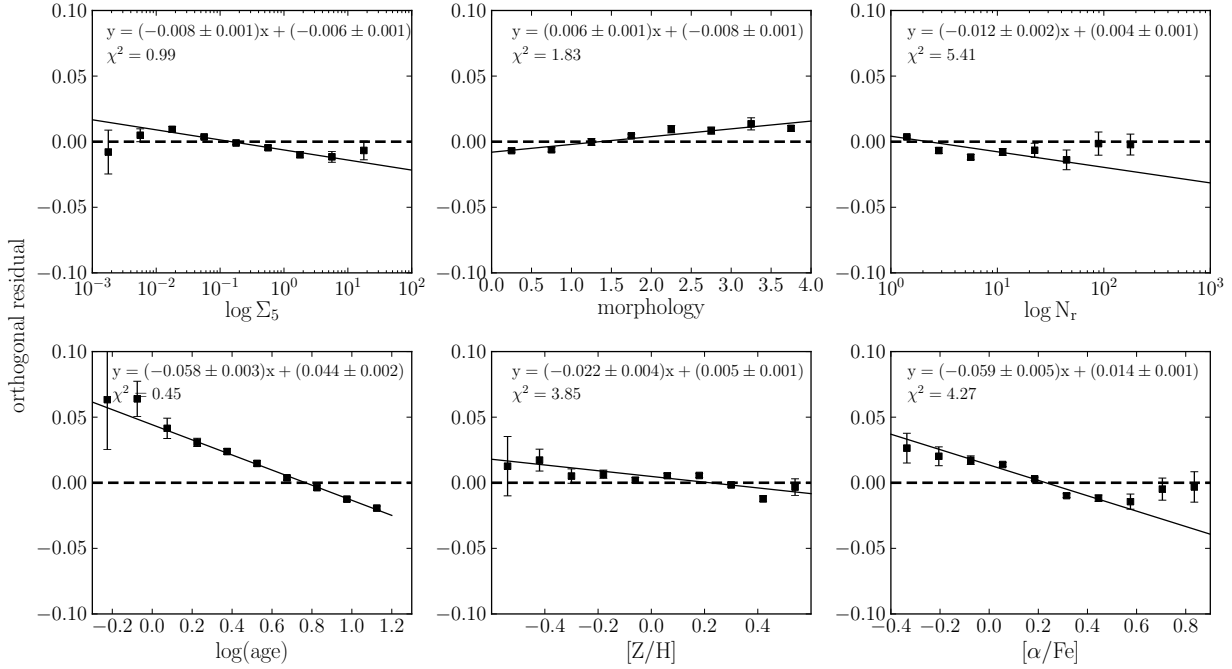
Figure 20. Correlation of orthogonal residuals relative to the best-fit FP ($a = 1.52$ and $b = -0.89$) with various galaxy properties: local density ($\log \Sigma_5$), morphological type and group richness ($\log N_R$) (all as defined in this paper), and $\log$ age, [Z/H] and [α/Fe] (as defined in Springob et al. 2012). In each panel the best-fitting line for the binned residuals is given along with the corresponding reduced χ^2 value.

tent with the E/S0 galaxy sample, although the FPs are offset in the sense that, at fixed velocity dispersion and surface brightness, early-type Sp bulges are on average about 10% larger than E/S0 galaxies. Contrary to our expectations, this does not appear to be a selection effect. Since the 6dFGS FP sample is dominated by E/S0 galaxies (6956 E/S0's and 1945 Sp bulges), the additional scatter in the overall FP from the offset in the FPs of the two types of galaxies is negligible.

Complementing the analysis of Springob et al. (2012), we determine the trends in the residuals of the FP as functions of group richness, local density, morphology, and the age, metallicity and α-enhancement of the stellar population. We find that the strongest trend is with age, and we speculate that, of the galaxy properties considered here, age is the most important systematic source of offsets from the FP, and may drive (through the correlations of age with environment, morphology and metallicity) most of the variations with the other galaxy properties. Demonstrating that this is the case, however, requires detailed analysis of the covariances between all these quantities, which we defer to a future paper.

The contributions to the intrinsic scatter about the FP from the mix of morphologies, environments and stellar populations present in the 6dFGS sample are at most (in the case of the ages of the stellar populations) a few percent. Although it is in principle possible to compensate for these effects, any corrections based on the mean relations between FP residuals and the properties of individual galaxies would in practice introduce more scatter than they would remove, due to the substantial uncertainties in determining these properties. In any case, the bulk of the intrinsic scatter would appear to be due either to physical parameters not considered here or to genuinely stochastic variations in the structure of galaxies.

Nonetheless, the systematic offsets of the FP for galaxies with different morphologies, environments and stellar populations are significant, and will need to be accounted for when, in future papers, we use these FP determinations to derive distances and peculiar velocities for this sample of $\sim 10^4$ early-type galaxies covering most of the southern hemisphere and reaching out to 16500 km s^{-1}.

REFERENCES

Barnes D. G., Fluke C. J., 2008, in Astronomical Society of the Pacific Conference Series, Vol. 394, Astronomical Data Analysis Software and Systems XVII, R. W. Argyle, P. S. Bunclark, & J. R. Lewis, ed., pp. 149–+

Barnes D. G., Fluke C. J., Bourke P. D., Parry O. T., 2006, PASA, 23, 82

Bender R., Burstein D., Faber S. M., 1992, ApJ, 399, 462

Bernardi M. et al., 2003, AJ, 125, 1866

Bruzual G., Charlot S., 2003, MNRAS, 344, 1000

Burstein D., Bender R., Faber S., Nolthenius R., 1997, AJ, 114, 1365

Burstein D., Faber S. M., Dressler A., 1990, ApJ, 354, 18

Busarello G., Capaccioli M., Capozziello S., Longo G., Puddu E., 1997, A&A, 320, 415

Campbell L., 2009, PhD thesis, Australian National University

Cappellari M. et al., 2006, MNRAS, 366, 1126

Ciotti L., Lanzoni B., Renzini A., 1996, MNRAS, 282, 1

Colless M., Jones H., Campbell L., Burkey D., Taylor A., Saunders W., 2005, in IAU Symposium, Vol. 216, Maps of the Cosmos, M. Colless, L. Staveley-Smith, & R. A. Stathakis, ed., pp. 180–189

Colless M., Saglia R. P., Burstein D., Davies R. L., McMahan R. K., Wegner G., 2001, MNRAS, 321, 277

de Carvalho R. R., Djorgovski S., 1992, ApJL, 389, L49

Desroches L.-B., Quataert E., Ma C.-P., West A. A., 2007, MNRAS, 377, 402

Djorgovski S., Davis M., 1987, ApJ, 313, 59

D'Onofrio M. et al., 2008, ApJ, 685, 875

D'Onofrio M., Valentinuzzi T., Secco L., Caimmi R., Bindoni D., 2006, New Astronomy Reviews, 50, 447

Dressler A., Lynden-Bell D., Burstein D., Davies R. L., Faber S. M., Terlevich R., Wegner G., 1987, ApJ, 313, 42

Eke V. R., Baugh C. M., Cole S., et al., 2004, MNRAS, 348, 866

Faber S. M., Jackson R. E., 1976, ApJ, 204, 668

Gargiulo A. et al., 2009, MNRAS, 397, 75

Gibbons R. A., Fruchter A. S., Bothun G. D., 2001, AJ, 121, 649

Graham A., Colless M., 1997, MNRAS, 287, 221

Graves G. J., Faber S. M., 2010, ApJ, 717, 803

Graves G. J., Faber S. M., Schiavon R. P., 2009, ApJ, 698, 1590

Graves G. J., Faber S. M., Schiavon R. P., 2010, ApJ, 721, 278

Guzman R., Lucey J. R., Bower R. G., 1993, MNRAS, 265, 731

Hambly N. C. et al., 2001, MNRAS, 326, 1279

Hogg D. W., Bovy J., Lang D., 2010, ArXiv Astrophysics e-prints, arXiv:1008.4686

Hudson M. J., Lucey J. R., Smith R. J., Steel J., 1997, MNRAS, 291, 488

Hudson M. J., Smith R. J., Lucey J. R., Branchini E., 2004, MNRAS, 352, 61

Hyde J. B., Bernardi M., 2009, MNRAS, 396, 1171

Jarrett T. H., Chester T., Cutri R., Schneider S., Skrutskie M., Huchra J. P., 2000, AJ, 119, 2498

Jones D. H. et al., 2009, MNRAS, 399, 683

Jones D. H. et al., 2004, MNRAS, 355, 747

Jones D. H., Saunders W., Read M., Colless M., 2005, PASA, 22, 277

Jorgensen I., Franx M., Kjaergaard P., 1995, MNRAS, 276, 1341

Jorgensen I., Franx M., Kjaergaard P., 1996, MNRAS, 280, 167

Jun H. D., Im M., 2008, ApJL, 678, L97

Kormendy J., 1977, ApJ, 218, 333

Korn A. J., Maraston C., Thomas D., 2005, A&A, 438, 685

Kourkchi E., Khosroshahi H. G., Carter D., Mobasher B., 2012, MNRAS, 420, 2835

La Barbera F., Busarello G., Merluzzi P., de la Rosa I. G., Coppola G., Haines C. P., 2008, ApJ, 689, 913

La Barbera F., de Carvalho R. R., de La Rosa I. G., Lopes P. A. A., 2010a, MNRAS, 408, 1335

La Barbera F., de Carvalho R. R., de La Rosa I. G., Lopes P. A. A., Kohl-Moreira J. L., Capelato H. V., 2010b, MNRAS, 408, 1313

La Barbera F., Lopes P. A. A., de Carvalho R. R., de La Rosa I. G., Berlind A. A., 2010c, MNRAS, 408, 1361

Lucey J. R., Bower R. G., Ellis R. S., 1991, MNRAS, 249, 755

Lucey J. R., Guzman R., Carter D., Terlevich R. J., 1991, MNRAS, 253, 584

Maraston C., 2005, MNRAS, 362, 799

Müller K. R., Freudling W., Watkins R., Wegner G., 1998, ApJL, 507, L105

Nelder J., Mead R., 1965, The Computer Journal, 7, 308

Nigoche-Netro A., Aguerri J. A. L., Lagos P., Ruelas-Mayorga A., Sánchez L. J., Machado A., 2010, A&A, 516, A96+

Nigoche-Netro A., Ruelas-Mayorga A., Franco-Balderas A., 2008, A&A, 491, 731

Pahre M. A., de Carvalho R. R., Djorgovski S. G., 1998, AJ, 116, 1606

Pahre M. A., Djorgovski S. G., de Carvalho R. R., 1998, AJ, 116, 1591

Peng C. Y., Ho L. C., Impey C. D., Rix H.-W., 2002, AJ, 124, 266

Powell M. J. D., 2006, in "Large-Scale Nonlinear Optimization", Roma, M. and Di Pillo, G., ed., Springer, New York, pp. 255–297

Reda F. M., Forbes D. A., Hau G. K. T., 2005, MNRAS, 360, 693

Saglia R. P., Bender R., Dressler A., 1993, A&A, 279, 75

Saglia R. P., Colless M., Burstein D., Davies R. L., McMahan R. K., Wegner G., 2001, MNRAS, 324, 389

Schmidt M., 1968, ApJ, 151, 393

Schwarz G., 1978, Ann. Statist., 6, 461

Scodeggio M., Gavazzi G., Belsole E., Pierini D., Boselli A., 1998, MNRAS, 301, 1001

Scodeggio M., Giovanelli R., Haynes M. P., 1997, AJ, 113, 101

Springob C. M. et al., 2012, MNRAS, 420, 2773

Strauss M. A., Willick J. A., 1995, Phys. Rep., 261, 271

Tonry J., Davis M., 1979, AJ, 84, 1511

Trujillo I., Burkert A., Bell E. F., 2004, ApJL, 600, L39

Worthey G., 1994, ApJS, 95, 107

APPENDIX A: LIKELIHOOD NORMALISATION

For a trivariate Gaussian with lower selection limits of r_{cut}, s_{cut} and i_{cut}, the likelihood normalisation integral is

$$f_n = \int_{r_{cut}}^{\infty} \int_{s_{cut}}^{\infty} \int_{u_{cut}}^{\infty} \frac{\exp[\frac{1}{2}(\mathbf{x_n^T}(\mathbf{\Sigma} + \mathbf{E_n})^{-1}\mathbf{x_n})]}{\sqrt{(2\pi)^3|\mathbf{\Sigma} + \mathbf{E_n}|}} \, dx \quad \text{(A1)}$$

where $\mathbf{x_n} = (r_n, s_n, i_n)$. To determine f_n numerically, we transform the integral using the Cholesky decomposition of the matrix sum $\mathbf{\Sigma} + \mathbf{E_n} = \mathbf{C}$ and then again using the standard normal distribution function, $\Phi(y)$, given by

$$\Phi(y) = \frac{1}{2\pi} \int_{-\infty}^{y} \exp^{-\frac{1}{2}\theta^2} \, d\theta \quad \text{(A2)}$$

A final substitution is made to perform the integration over a unit cube, resulting in the integral

$$
\begin{aligned}
f_n = (1 - &\Phi(\frac{r_{cut}}{C_{00}})) \\
&\times \int_0^1 (1 - \Phi[\frac{s_{cut}}{C_{11}} - \frac{C_{10}}{C_{11}}\Phi^{-1}((1-w_0)\Phi(\frac{r_{cut}}{C_{00}}) + w_0)]) \\
&\times \int_0^1 (1 - \Phi[\frac{u_{cut}}{C_{22}} - \frac{C_{20}}{C_{22}}\Phi^{-1}((1-w_0)\Phi(\frac{r_{cut}}{C_{00}}) + w_0) \\
&- \frac{C_{21}}{C_{22}}\Phi^{-1}((1-w_1)\Phi[\frac{s_{cut}}{C_{11}} \\
&- \frac{C_{10}}{C_{11}}\Phi^{-1}((1-w_0)\Phi(\frac{r_{cut}}{C_{00}}) + w_0)] + w_1)]) \int_0^1 d\mathbf{w}
\end{aligned}
$$

$$(\text{A3})$$

In practice our model only includes an explicit selection cut in velocity dispersion ($\sigma \geqslant \sigma_{cut}$). The above equation then reduces to

$$
f_n = \int_0^1 1 - \Phi[\frac{s_{cut}}{C_{11}} - \frac{C_{10}}{C_{11}}\Phi^{-1}(w_0)] \, dw_0 \qquad (\text{A4})
$$

APPENDIX B: INTERACTIVE 3D FIGURES

Several of the figures presented here (namely Figures 3, 9, 12, 14 and 17) can be accessed as 3D interactive visualisations when viewing this paper in Acrobat Reader v8.0 or higher. Once 3D viewing is enabled by clicking on the figure, the 3D mode allows the reader to rotate, pan and zoom the view using the mouse.

The toolbar on each 3D figure contains a whole host of interactive elements which can help in exploring the 3D visualisation. We particularly direct the reader's attention to the following toolbar features: (i) you can restore the initial default view at any time using the home button; (ii) you can rotate to any orientation you prefer and, where relevant, to special, author-selected 3D views (e.g. the edge-on view of the FP); these can be selected from the Views drop-down menu; (iii) you can toggle the model tree, which allows individual plot features (e.g. scatter points, planes, vectors) of the 3D figure to be turned on and off, giving the viewer greater control of the interactive figure. Suggested interactions with particular 3D figures include:

(a) In Figure 3, use the model tree to toggle the $\mathbf{v}$-space vectors and mass/luminosity vectors one at a time to see how they compare in our 3D Gaussian model. Also, rotate the figure to view the small angle between $\mathbf{v_1}$ and $\mathbf{m} - \mathbf{l}$ and also $\mathbf{v_2}$ and $\mathbf{l} - 3\mathbf{r}$.

(b) Figure 9 not only contains the J band FP sample of galaxies, but also the H band and K band samples. They can be enabled in the model tree by selecting 'H Band' or 'K Band' respectively. For an unimpeded view of the individual galaxies, toggle the best-fit plane (called 'Fundamental Plane' in the model tree); this also applies to Figures 14 and 17. In the Views drop-down menu, select 'Edge-on' to view the Fundamental Plane in the projection with the smallest scatter.

(c) In Figure 14, rotate and pan across the FP galaxies to explore where the richness subsamples lie on the Fundamental Plane.

(d) In Figure 17, toggle the individual points of each morphology subsample to see the differences in the way their distributions populate FP space.